

LA-ICP-MS titanite U-Pb dating and mineral chemistry of the Luohé magnetite-apatite (MA)-type deposit in the Lu-Zong volcanic basin, Eastern China



Yinan Liu^{a,b}, Yu Fan^{a,b,*}, Taofa Zhou^{a,b}, Lejun Zhang^c, Noel C. White^{a,b,c}, Haolan Hong^{a,b}, Wei Zhang^{a,b}

^a School of Resources and Environmental Engineering, Hefei University of Technology, Hefei 230009, China

^b Ore Deposit and Exploration Centre, Hefei University of Technology, Hefei 230009, China

^c Centre of Excellence in Ore Deposits (CODES), University of Tasmania, Private Bag 79, Hobart, Australia

ARTICLE INFO

Keywords:

Luohe Fe deposit
Lu-Zong volcanic basin (Eastern China)
Middle-Lower Yangtze River Valley
Metallogenic Belt (MLYB)
Magnetite-apatite (MA) metallogeny
Titanite U-Pb dating

ABSTRACT

The Luohe Fe deposit is the largest magnetite-apatite (MA)-type deposit in the Middle-Lower Yangtze River Valley Metallogenic Belt (MLYB) (around 1 Gt Fe ore resource). The main orebody is hosted by volcanic rocks, and widespread titanite mineralization is developed in the footwall of the shallow ore bodies, and in the hanging wall of the deep ore bodies. Trace element chemistry of the well-crystallized hydrothermal titanite from both deep and shallow ore bodies indicates coupled substitution of $(\text{Al}, \text{Fe})^{3+} + (\text{F}, \text{OH})^-$ for $\text{Ti}^{4+} + \text{O}^{2-}$, and the addition of elements such as Zr, Nb and REEs. Titanite Zr-thermometry yielded a mineralization temperature of ca. 700 °C, suggesting that the Luohe magnetite-apatite deposit was formed at a higher temperature than typical Fe skarn deposits in the metallogenic belt. The high ore-forming temperature may have been a key factor in Ti migration. The distinct LREE enrichment, the relatively high total REE concentrations, and the marked negative Eu anomalies all suggest that the Luohe titanite may have crystallized before apatite and epidote in a high-temperature hydrothermal environment. Variation in the negative Eu anomalies suggests the ore fluid oxygen fugacity increased from deep to shallow levels. Our study suggests that the Th/U ratio is not an efficient igneous vs. hydrothermal titanite discriminator for high-temperature titanite. LA-ICP-MS titanite U-Pb dating of the shallow and deep orebodies yielded ages of 130.0 ± 0.9 Ma and 129.1 ± 0.8 Ma to 129.7 ± 0.8 Ma, consistent with the age of the deep-seated diorite in the area. We propose that the shallow- and deep-level orebodies at Luohe were deposited from the same mineralizing system and mineralization was closely related to the deep-seated diorite.

1. Introduction

Titanite (CaTiSiO_5) is a common accessory mineral in magmatic and metamorphic rocks and in hydrothermal ore deposits. Titanite contains relatively high rare earth element (REE) and high field strength element (HFSE) concentrations (Tiepolo et al., 2002; Gao et al., 2012; Deng et al., 2015), and titanite of different origins displays different trace element geochemical characteristics (Gao et al., 2012; Che et al., 2013; Ismail et al., 2014; Cao et al., 2015; Xu et al., 2015) that can provide insights into its formation temperature, pressure and oxygen fugacity ($f\text{O}_2$) (Hayden et al., 2008; Mazdab, 2009; Che et al., 2013; Ismail et al., 2014; Xu et al., 2015).

Titanite commonly contains high U, Th, and low common lead concentrations, so it can be precisely dated (Aleinikoff et al., 2002;

Storey et al., 2006, 2007). Titanite is more susceptible to high temperature hydrothermal alteration than zircon, making titanite suitable for recording complex magmatic, metamorphic and hydrothermal processes (Scott and St-Onge, 1995; Chiaradia et al., 2009). Titanite U-Pb ages obtained in each thermal stage are likely to represent crystallization (instead of merely thermal resetting) events (Corfu and Grunsky, 1988; Aleinikoff et al., 2002). These advantages have given titanite U-Pb geochronology increasing popularity in dating magmatic and hydrothermal events (e.g., Aleinikoff et al., 2002; Storey et al., 2007; Chiaradia et al., 2009; Smith et al., 2009; Li et al., 2010; Sun et al., 2010; Kohn and Corrie, 2011; Zhu et al., 2014; Fallour et al., 2014; Sepahi et al., 2014; Bonamici et al., 2015; Chelle-Michou et al., 2015; Deng et al., 2015; Fu et al., 2016). Recent research on hydrothermal titanite has mainly focused on skarn-type deposits, whereas

* Corresponding author at: School of Resources and Environmental Engineering, Hefei University of Technology, Hefei 230009, China.
E-mail address: fanyu@hfut.edu.cn (Y. Fan).

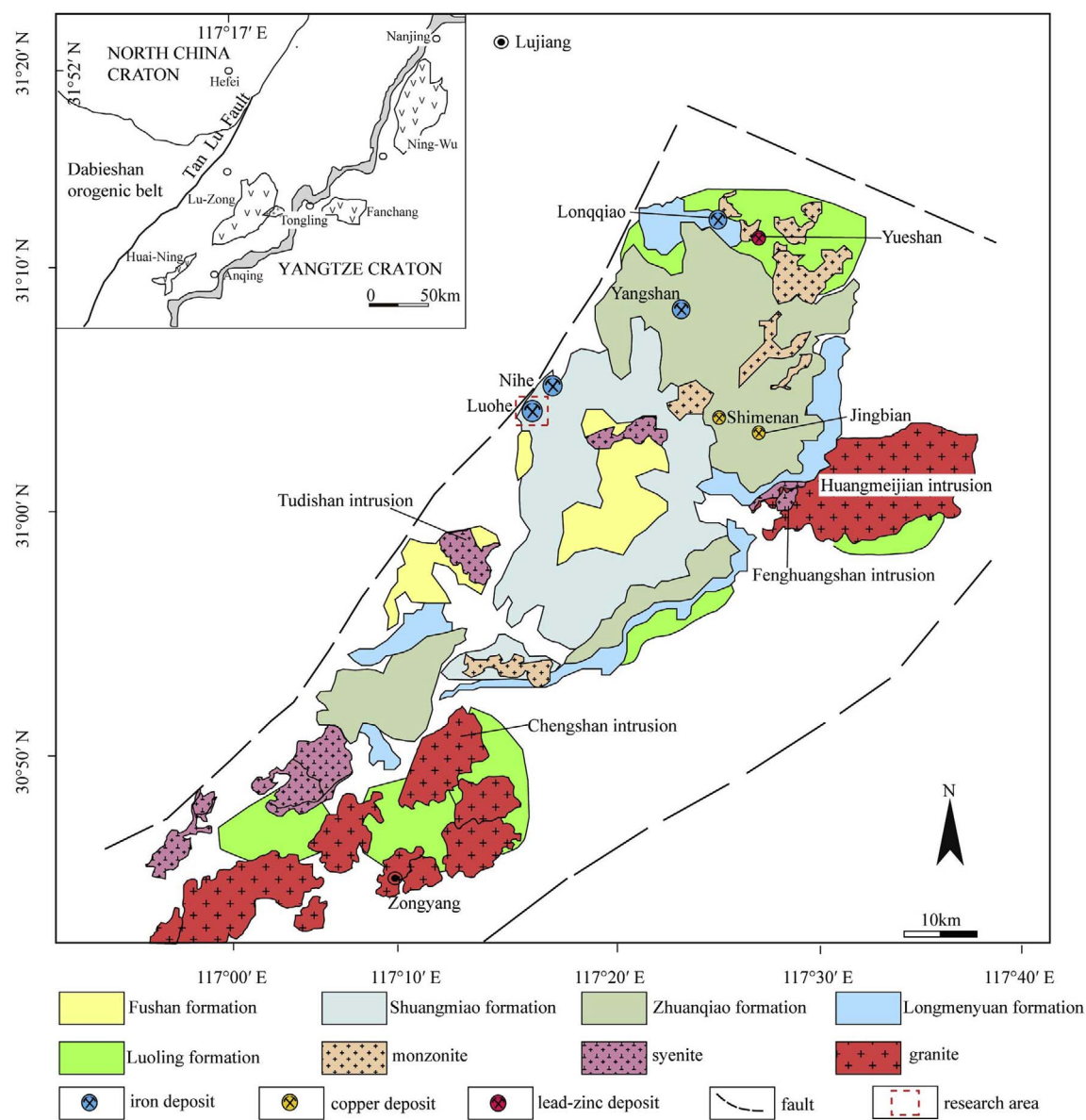


Fig. 1. Geologic sketch map of the Lu-Zong volcanic basin (after Zhou et al., 2010a,b).

magnetite-apatite (MA)-type deposits have rarely been reported.

The MLYB is an important polymetallic mineral province in Eastern China. Previous geochronology studies in the area have focused on zircon U-Pb dating of the related intrusions and Ar-Ar dating of hydrothermal phlogopite to determine the age of MA-type deposits; U-rich minerals in the deposits, such as titanite, have previously attracted little attention. This dating strategy has the problems that the intrusion age need not be the age of mineralization, and the closure temperature of phlogopite for Ar-Ar dating is relatively low (400–480 °C, Dodson, 1973; Giletti and Tullis, 1977), so that it does not accurately reflect the age of the magnetite-apatite deposit, which formed at high temperature. Titanite has a high closure temperature (650–700 °C, Pidgeon et al., 1996), so it is an ideal mineral for dating magnetite-apatite type deposits.

Luohe is the largest MA deposit in the MLYB. Qin et al. (2010) reported a zircon U-Pb age of volcanic rocks in the Luohe deposit (133 Ma), but the ore-forming age has not previously been determined with precision. In this paper we report detailed geology of Luohe deposit, and new geochronological and mineral chemical data for titanite from the deep and shallow orebodies. We compare titanite geochemical

characteristics from Luohe to titanite in other deposits in the MLYB, discuss the spatial-temporal distribution of the MA deposits in the Lu-Zong basin, and provide new insights into the ore genesis of the MA deposits like Luohe of the region.

2. Geological background

The Mesozoic Lu-Zong volcanic basin is one of the most important mineral districts in the middle MLYB (Chang et al., 1991; Zhai et al., 1992; Tang et al., 1998; Fan et al., 2008; Zhou et al., 2007, 2008a,b, 2010a,b, 2011a,b; Dong et al., 2010; Yuan et al., 2008). The MLYB belt hosts around 200 Fe, Cu and Au deposits (Pan and Dong, 1999; Mao et al., 2006; Zhou et al., 2008a,b, 2012). Shoshonitic volcanic rock and igneous intrusions are widespread in the basin, along with many Fe (-Cu-Pb-Zn-U) deposits (Liu et al., 2002; Xie et al., 2009). The host lithostratigraphy comprises the Middle Jurassic Luoling Formation terrigenous clastic sedimentary rocks, which are overlain unconformably by volcanic rocks comprising (from old to young) the Longmenyuan, Zuanqiao, Shuangmiao and Fushan formations. They are exposed in a synclinal structure and are separated by unconformities. Each volcanic

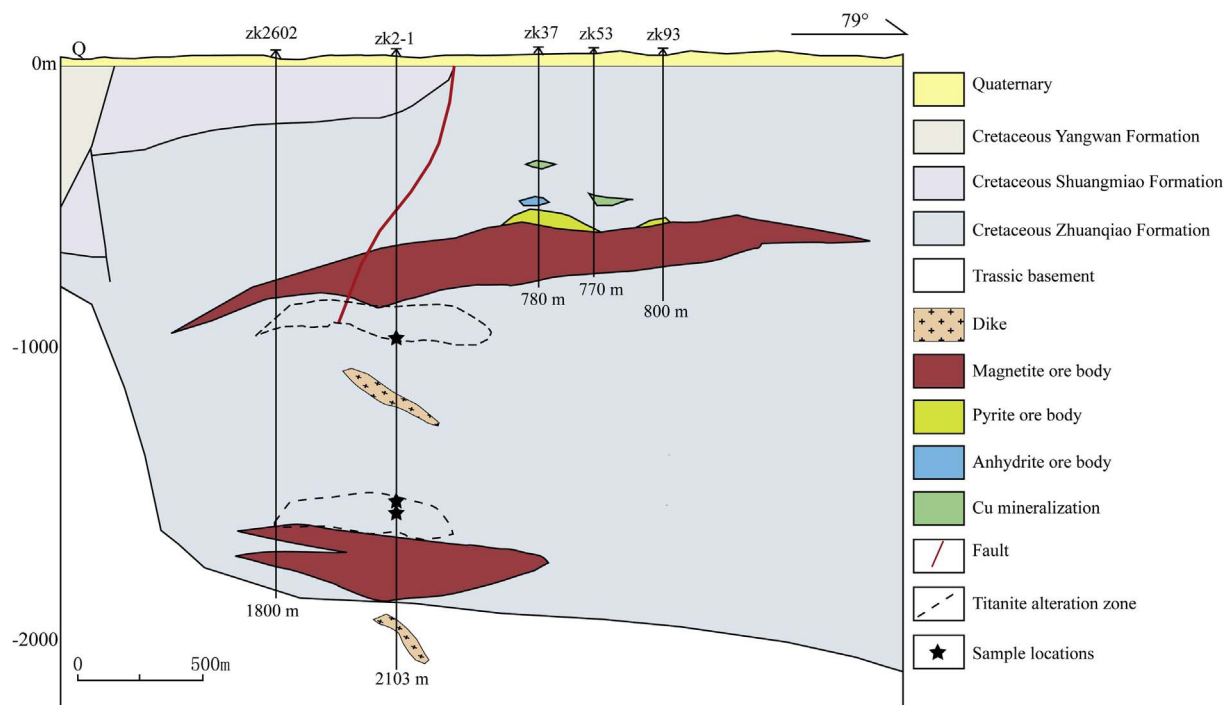


Fig. 2. Geological section of No. 2 prospecting line in Luohé iron deposit.

cycle commenced with eruptive facies, followed by increasing lava flows and ended with volcano-sedimentary facies. The volcanic eruptions are interpreted to have evolved from fissure-central vent style to typical central vent style (Ren et al., 1991; Zhou et al., 2008a,b). Intrusions are closely related to the regional volcanism, and occurred during late-stage volcanism, or intermittent volcanic quiescence. Around 34 exposed igneous intrusions have been documented, and include four types: namely, (1) buried diorite (in the northern Lu-Zong basin), including the Longqiao and Makou plutons; (2) monzonite (in the northern Lu-Zong basin), including the Bajiatan, Xiewani and Luoling plutons; (3) syenite, including the Tudishan and Fenghuangshan plutons; (4) A-type granite, including the Chengshan, Huashan and Huangmeijian plutons (Fan et al., 2008; Zhou et al., 2010a,b). Major mineral deposits in the Lu-Zong basin include Fe (e.g., Luohé, Longqiao and Nihe), Pb-Zn-Ag (Yueshan), small hydrothermal Cu-Au deposits (e.g., Jingbian-Shimen'an, Tiantoushan and Bamaoshan), alunite deposit (Fanshan) and Fe-oxide-Cu-Au-(U) deposits/occurrences (e.g., Yangqiao and Wuqiao). Total Fe ore resources are estimated to be 1.5 Gt, hosted primarily in the Zhuanqiao formation (except Longqiao skarn deposit which is hosted in the Triassic calcareous siltstone). Albitization is widespread, and the magnetite orebodies contain clinopyroxene and apatite.

Luohe, the largest magnetite-apatite deposit in the MLYB, is located in the western Lu-Zong basin (Fig. 1). Discovered in the 1970s at 400–700 m depth, the deposit contains west-dipping stratiform and lensoidal orebodies. Deep-level (1350–1800 m deep) stratiform orebodies (ca. 1260 m long, 840 m wide, 76 m thick on average) were discovered in 2013. The shallow- and deep-level orebodies contain a resource of ca. 1 Gt of iron ore with an average grade of 35 wt% Fe (Gao et al., 2013). Two titanite-bearing alteration zones occur at Luohe, containing large amounts of well-crystallized titanite, which provides a proxy for determining the magnetite-apatite mineralization age and ore fluid evolution.

The Luohe mining district is mainly covered by Quaternary

sediments with local outcrops of the Cretaceous Shuangmiao and Zhuanqiao formations consisting of trachytic lavas and volcanoclastic rocks (Fig. 2). Deep drill-holes have intersected Middle Triassic (T_2d) Dongma'anshan Formation of limestone-gypsum interbeds at 2000–2200 m. Laminated sedimentary rocks of the Dongma'anshan Formation make up the basement of the Lu-Zong basin, with the gypsum being partially converted to anhydrite. The structural geology at Luohe is simple, with gently dipping strata cut by some steeply dipping faults, which slightly drag the strata. Two sets of horizontal conjugate fractures are closely related to the alteration and mineralization, with vein stockwork orebodies mainly filling-in or replacing the wall rocks along these fractures (Huang, 1989). No large intrusions have been found at Luohe; there are minor post-mineralization trachyte porphyry and microcrystalline syenite dykes (Fig. 2). The steeply dipping fine-grained syenite intruded the Zhuanqiao Formation, and the trachyte porphyry intruded the Triassic Dongma'anshan Formation. Geochemical analysis of the Na-altered and fresh trachy-andesite indicates that the Na-alteration was unlikely to leach sufficient Fe from the trachy-andesite, and that the ore fluids were probably derived from deep dioritic intrusions (Liu, 2015).

Alteration minerals at Luohe include diopside, phlogopite, anhydrite, epidote, fluorapatite and titanite. Based on their crosscutting and replacement relationships the Luohe alteration/mineralization can be divided into the following stages: Stage I, alkali feldspar; Stage II, diopside-anhydrite-magnetite; Stage III, hematite-carbonate; Stage IV, anhydrite-pyrite; Stage V, quartz-sulfide; and Stage VI, carbonate-anhydrite vein (Liu et al., 2016). The titanite samples in this study are from Stage II (the major Fe mineralization stage), and were collected from the footwall of the shallow orebody (ca. 900–1100 m depth) and the hanging wall of the deep orebody (ca. 1500–1600 m depth) (Fig. 2).

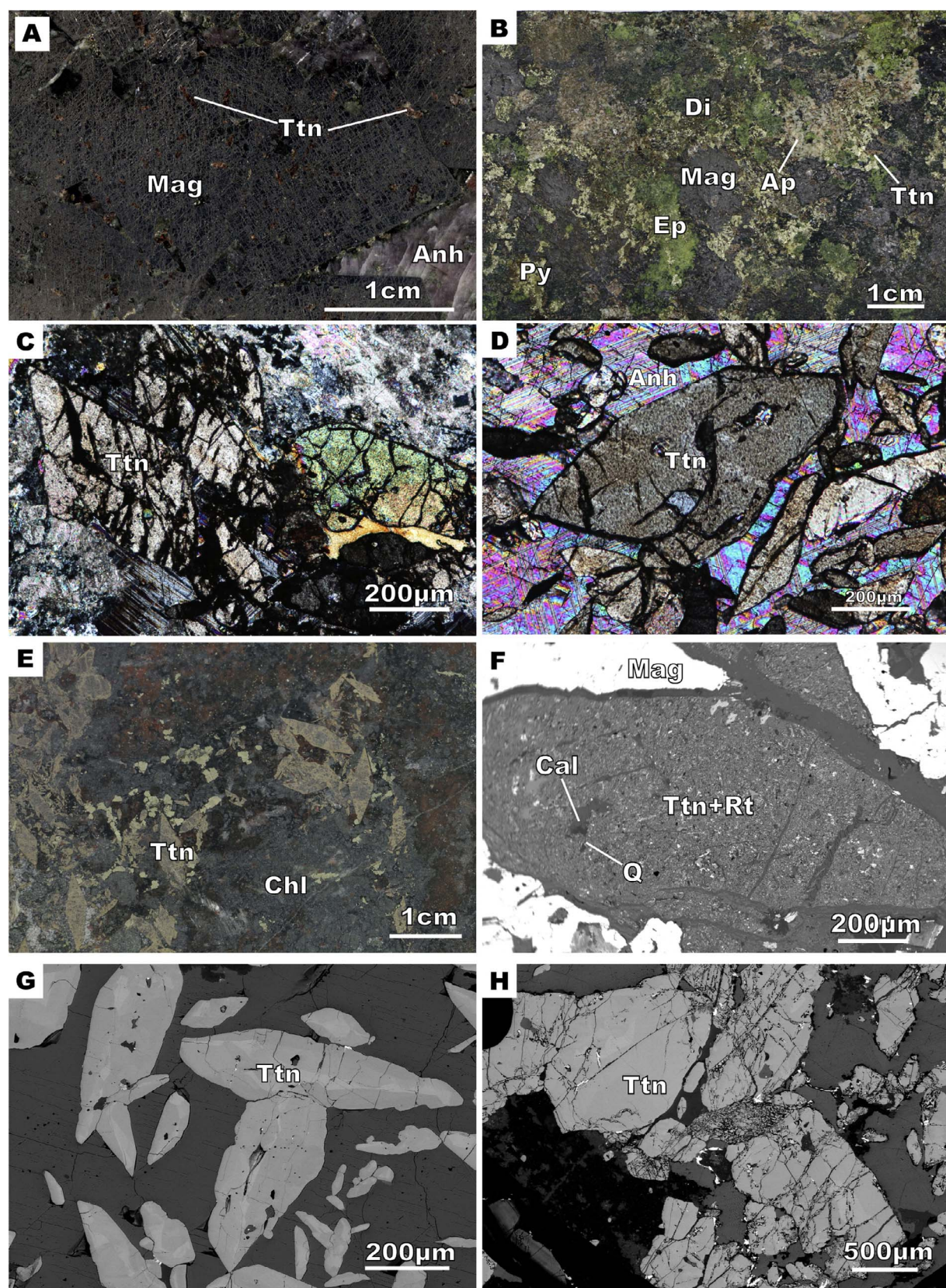


Fig. 3. Photographs (A–E) and BSE images (F–H) of the Luohu titanite: (A) Deep-level euhedral titanite in magnetite; (B) Deep-level titanite aggregate with magnetite, apatite and chloritized diopside; (C) Euhedral titanite in diopside-anhydrite vein (Zk2-1-1500); (D) Euhedral titanite in diopside-anhydrite vein (Zk2-1-1547); (E) Shallow-level euhedral yellow titanite with chlorite (Zk2-1-1092); (F) Altered titanite consisting of fine-grained rutile, quartz and calcite (Zk2-1-1092, BSE image); (G) Deep-level fresh euhedral titanite with anhydrite (Zk2-1-1500, BSE image); (H) Shallow-level relatively fresh titanite (Zk2-1-1092, BSE image). Abbreviations: Anh – Anhydrite; Ap – Apatite; Cal – Calcite; Chl – Chlorite; Di – Diopside; Ep – Epidote; Mag – Magnetite; Py – Pyrite; Q – Quartz; Rt – Rutile; Ttn – Titanite.

Table 1

Electron microprobe analysis results (wt%) of the Luohetitanite.

Sample No.	SiO ₂	TiO ₂	Al ₂ O ₃	FeO	MnO	MgO	CaO	Na ₂ O	K ₂ O	P ₂ O ₅	SO ₃	Cl	F	Total
<i>zk2-1-1092</i>														
1	30.11	35.23	1.26	1.96	0.03	0	27.95	0.01	0	0.07	0	0	0.83	97.06
2	30.28	35.11	1.5	2.09	0.01	0.02	28.15	0.02	0.01	0.04	0	0	0.86	97.71
3	30.08	35.82	1.09	1.63	0.01	0.01	27.91	0.01	0	0.03	0	0	0.58	96.94
4	30.33	35.47	1.35	2.06	0.01	0	27.83	0.01	0	0.03	0.01	0	0.77	97.54
5	30.07	35.68	1.19	1.77	0	0.02	27.77	0	0	0.05	0.01	0.01	0.69	96.96
6	30.16	35.22	1.26	2.06	0.04	0.01	27.78	0.04	0	0.06	0	0	0.77	97
7	30.48	35.16	1.67	2.2	0.03	0.03	28.29	0.02	0	0.03	0	0	0.86	98.41
8	30.16	36.42	1.07	1.53	0.01	0.01	27.74	0	0.01	0.05	0.08	0	0.58	97.41
9	30.65	35.79	1.46	2.07	0	0.01	28.08	0.01	0	0.02	0.01	0.01	0.79	98.51
10	30.52	35.4	1.35	1.82	0.02	0	27.85	0	0.01	0.05	0.01	0.01	0.79	97.46
11	30.58	35.81	1.41	2.07	0.02	0	28.06	0	0	0.05	0.02	0	0.78	98.47
12	30.27	34.96	1.21	1.82	0.01	0.01	27.55	0.03	0	0.06	0.02	0	0.74	96.34
13	30.01	35.47	1.28	1.92	0.03	0.02	27.8	0.01	0	0.06	0.01	0	0.83	97.09
14	30.18	35.38	1.38	1.83	0.01	0	27.72	0.06	0	0.05	0.01	0	0.77	97.07
<i>zk2-1-1500</i>														
1	29.87	34.8	1.46	2.05	0.02	0.03	27.06	0.02	0.01	0.13	0.01	0.01	0.66	95.81
2	30.12	35.03	1.47	1.9	0.01	0.01	27.6	0.01	0	0.06	0.02	0	0.82	96.65
3	29.66	35.1	1.41	1.58	0.01	0.01	27.11	0	0.01	0.07	0	0.01	0.59	95.25
4	29.93	33.98	1.99	2.02	0	0.02	27.5	0	0.01	0.02	0.01	0	0.9	95.99
5	30.18	35.05	1.48	1.85	0.03	0.02	27.52	0.01	0	0.05	0.01	0	0.84	96.69
6	29.98	34.57	1.96	1.95	0.01	0	27.58	0.01	0.02	0.07	0	0	1.01	96.67
7	30	34.78	1.88	1.71	0.02	0.02	27.73	0.01	0.01	0.02	0.02	0	1.04	96.79
8	29.7	35.13	1.34	1.91	0.01	0	27.37	0	0.01	0.11	0	0	0.75	95.99
9	29.84	34.44	1.74	1.94	0.02	0.02	27.71	0.01	0	0.05	0.03	0	0.95	96.35
10	29.83	35.21	1.53	1.67	0.02	0.02	27.32	0.02	0.01	0.1	0	0	0.7	96.12
11	30.08	34.81	1.58	1.92	0.01	0	27.51	0.02	0	0.05	0	0	0.79	96.39
12	29.93	34.86	1.35	1.96	0	0	27.26	0.01	0.01	0.09	0.01	0	0.63	95.83
13	29.69	35.69	1.34	1.89	0	0.01	27.32	0.02	0.01	0.12	0.01	0	0.65	96.47
14	30.19	36.03	1.3	1.85	0.02	0	27.72	0.01	0.01	0.08	0.01	0	0.67	97.59
15	29.87	35.88	1.32	2.03	0.02	0.01	27.44	0.01	0	0.15	0.03	0	0.7	97.08
16	30.31	36.03	1.36	1.8	0.03	0.01	27.94	0	0.01	0.06	0	0	0.74	97.96
17	29.71	35.26	1.32	2.11	0.01	0.01	27.13	0.01	0.01	0.16	0	0	0.57	96.08
18	30.14	35.75	1.14	1.63	0	0.01	27.7	0.02	0	0.04	0	0	0.66	96.79
19	30	35.34	1.74	1.74	0.03	0.01	27.24	0.02	0.01	0.17	0	0	0.66	96.68
20	30.14	35.97	1.09	1.54	0.03	0.01	27.62	0.05	0	0.05	0.01	0	0.56	96.83
21	30.08	35.16	1.21	1.88	0.01	0.01	27.33	0.02	0	0.08	0	0.01	0.58	96.14
22	30.25	35.78	1.13	1.54	0.02	0.01	27.6	0.04	0.01	0.04	0	0	0.58	96.73
23	30.12	34.72	1.74	2.12	0	0.01	27.83	0	0	0.05	0.02	0	1.01	97.17
24	30.13	34.98	1.59	2.16	0.01	0.01	27.88	0.03	0.01	0.03	0.01	0	0.74	97.27
<i>zk2-1-1547</i>														
1	29.88	36.76	1.52	1.38	0.01	0.01	27.84	0.06	0	0.04	0	0	0.55	97.81
2	30.55	35.95	1.47	1.74	0	0.04	28.49	0.05	0	0.05	0	0	0.85	98.83
3	30.25	37.14	0.94	1.43	0.03	0.01	28.02	0.01	0	0.04	0	0	0.52	98.17
4	30.37	36.26	1.19	1.49	0.03	0.01	27.86	0.02	0.01	0.05	0.01	0	0.67	97.65
5	30.3	36.58	1.21	1.33	0.02	0.01	27.93	0	0.01	0.05	0.02	0	0.62	97.77
6	30.07	35.44	1.58	1.8	0	0.01	27.51	0.01	0.01	0.1	0.01	0.01	0.83	97.03
7	29.96	35.17	1.42	1.83	0.02	0.01	27.45	0.02	0	0.06	0.01	0	0.66	96.34
8	30.65	35.46	1.36	1.64	0.01	0	27.7	0.01	0	0.04	0.05	0	0.7	97.29
9	30.04	36.41	1.17	1.54	0	0	27.79	0.01	0	0.03	0.02	0.01	0.67	97.41
10	30.09	35.92	1.68	1.86	0	0.02	28.3	0.04	0.01	0.04	0	0	0.81	98.42
11	30.2	34.85	2.1	1.92	0.01	0.01	28.26	0.01	0	0.05	0.01	0	0.96	97.96
12	30.55	35.83	1.74	1.73	0.02	0	28.05	0.04	0.01	0.03	0.01	0	0.9	98.46
13	30.06	35.33	1.88	2	0.03	0.01	27.83	0.02	0	0.09	0	0	0.75	97.67
14	29.69	35.19	2	1.83	0.01	0.01	28.03	0.02	0	0.07	0.02	0	1.06	97.42
15	30.03	34.7	1.97	2.04	0.01	0.02	27.71	0.05	0	0.1	0.01	0	0.88	97.15
16	30.34	34.24	2.1	2.13	0.01	0.02	27.95	0.02	0	0.03	0.01	0	0.9	97.35
17	30.06	34.79	1.76	2.12	0.03	0.01	27.74	0.03	0.01	0.14	0.01	0	0.66	97.05
18	30.22	34.91	1.62	2.12	0.02	0.01	27.85	0.01	0.01	0.06	0.01	0	0.77	97.24

3. Sampling and methods

3.1. Sampling

Three titanite samples were chosen for radiometric dating (sampling locations are shown in Fig. 2): Two of them (zk2-1-1500 and zk2-1-1547) were from diopside-anhydrite altered rocks in the hanging wall of the deep orebody. The titanite is euhedral (ca. 1–3 mm irregular rhombohedra) and brownish-yellow with adamantine luster. The titanite in samples zk2-1-1500 and zk2-1-1547 is relatively fresh, and

occurs in clusters with magnetite (locally as euhedral inclusions), diopside, epidote, apatite, and anhydrite (Fig. 3A–D). Sample zk2-1-1092 was from a chlorite-altered diopside-anhydrite-magnetite ore vein in the footwall of the shallow orebody. The euhedral-subhedral coarse-grained titanite (ca. 5–10 mm) is earthy-yellow and rhombohedral (Fig. 3E). The titanite coexists with diopside, anhydrite, chlorite and albite. Back-scattered electron (BSE) imaging reveals the presence of alteration minerals (e.g., rutile, calcite and quartz Fig. 3F) along fractures in the titanite, whereas fresh titanite (chosen for U-Pb dating in this study) is compositionally more homogenous (Fig. 3G, H).

Table 2Trace element analysis result ($\times 10^{-6}$) of the Luohé titanite by LA-ICP-MS.

Sample No.	La	Ce	Pr	Nd	Sm	Eu	Gd	Dy	Er	Yb	Zr	Nb	Σ REE	LREE/HREE	δ Eu	δ Ce
zk2-1-1092-1	1360	3519	433	1661	328	56	275	223	120	92	3199	1360	8067	10.4	0.57	1.16
zk2-1-1092-2	993	2613	320	1262	256	44	211	181	101	81	5833	865	6062	9.6	0.58	1.16
zk2-1-1092-3	746	2014	256	1036	214	38	190	166	93	72	1621	644	4825	8.3	0.58	1.16
zk2-1-1092-4	911	2497	320	1265	265	43	220	191	102	80	3647	863	5894	8.9	0.54	1.17
zk2-1-1092-5	764	2104	267	1072	222	40	190	167	91	72	2144	677	4989	8.6	0.60	1.18
zk2-1-1092-6	708	1915	249	990	211	38	183	162	92	75	1659	609	4623	8.0	0.59	1.16
zk2-1-1092-7	1219	3195	394	1534	303	51	246	203	108	81	8650	1359	7334	10.5	0.57	1.16
zk2-1-1092-8	883	2471	318	1298	274	42	228	197	105	83	6082	924	5899	8.6	0.51	1.18
zk2-1-1092-9	1314	3656	466	1808	356	57	286	231	121	91	5003	1312	8386	10.5	0.55	1.20
zk2-1-1092-10	758	2063	265	1070	225	39	189	165	89	72	2969	684	4935	8.6	0.58	1.16
zk2-1-1092-11	1325	3805	503	1992	397	63	318	255	135	100	5463	1256	8893	10.0	0.54	1.20
zk2-1-1092-12	700	1894	245	963	206	36	182	163	89	74	1473	539	4552	8.0	0.57	1.16
zk2-1-1092-13	1110	3055	387	1516	308	50	245	199	103	80	5213	978	7053	10.2	0.56	1.19
zk2-1-1092-14	1327	3352	417	1607	319	53	256	218	116	91	4728	1361	7756	10.4	0.57	1.13
zk2-1-1092-15	1119	3061	392	1527	314	47	247	203	106	79	5278	949	7095	10.2	0.52	1.18
zk2-1-1092-16	950	2616	333	1313	267	43	218	184	100	76	3480	836	6100	9.6	0.54	1.18
zk2-1-1092-17	862	2298	288	1139	234	39	194	164	90	69	2252	632	5377	9.4	0.56	1.16
zk2-1-1092-18	1017	2799	353	1394	282	48	233	191	100	75	4785	850	6492	9.8	0.57	1.18
zk2-1-1092-19	1026	2637	332	1290	260	44	216	182	99	77	4312	823	6163	9.7	0.57	1.14
zk2-1-1092-20	795	2175	274	1106	223	39	192	160	87	66	1651	550	5117	9.1	0.58	1.17
zk2-1-1092-21	838	2216	281	1131	236	40	194	171	90	72	3077	646	5269	9.0	0.57	1.14
zk2-1-1092-22	771	2112	271	1081	227	39	194	165	90	68	3597	686	5018	8.7	0.57	1.17
zk2-1-1092-23	1039	2921	379	1499	308	50	258	212	113	86	4505	1027	6865	9.3	0.54	1.19
zk2-1-1092-24	1083	3037	396	1581	319	51	259	212	112	86	3518	1012	7136	9.7	0.54	1.18
zk2-1-1092-25	1161	3054	380	1484	297	50	232	195	104	83	5946	1218	7040	10.5	0.58	1.16
zk2-1-1092-26	943	2597	332	1341	281	45	231	195	103	79	5893	1069	6148	9.1	0.54	1.17
zk2-1-1092-27	1020	2819	361	1454	302	49	240	210	110	82	4446	967	6646	9.4	0.55	1.17
zk2-1-1092-28	682	1876	238	966	207	36	185	160	89	73	1904	587	4512	7.9	0.56	1.17
zk2-1-1092-29	1063	2696	334	1293	263	45	220	187	101	80	3250	893	6282	9.7	0.57	1.14
zk2-1-1500-1	951	2786	363	1462	305	49	250	203	108	86	5417	1210	6563	9.1	0.54	1.21
zk2-1-1500-2	909	2777	360	1451	296	53	247	214	127	111	312	425	6545	8.4	0.60	1.25
zk2-1-1500-3	1092	3224	423	1674	333	55	271	227	128	107	918	730	7534	9.3	0.56	1.22
zk2-1-1500-4	1378	3815	485	1900	362	61	290	239	132	110	1299	884	8772	10.4	0.58	1.19
zk2-1-1500-5	1042	3079	394	1556	309	55	244	208	119	100	481	527	7106	9.6	0.61	1.24
zk2-1-1500-6	1116	3280	423	1663	333	56	273	231	134	115	406	698	7624	9.1	0.57	1.23
zk2-1-1500-7	1123	3363	436	1734	343	54	269	222	123	99	1494	677	7766	9.9	0.54	1.24
zk2-1-1500-8	1458	4045	512	1955	372	63	293	233	127	107	1006	805	9165	11.1	0.58	1.20
zk2-1-1500-9	1521	4213	531	2049	389	66	308	248	144	120	1195	1241	9589	10.7	0.58	1.20
zk2-1-1500-10	1356	3811	483	1874	361	60	280	228	126	106	484	726	8685	10.7	0.58	1.21
zk2-1-1500-11	1211	3563	461	1822	360	64	293	247	143	125	720	656	8289	9.3	0.60	1.23
zk2-1-1500-12	1229	3707	484	1906	374	65	297	243	131	113	1586	959	8549	9.9	0.60	1.25
zk2-1-1500-13	1370	3934	502	1959	377	64	292	234	130	109	748	919	8971	10.7	0.59	1.22
zk2-1-1500-14	1182	3415	431	1644	320	54	247	205	115	97	906	789	7710	10.6	0.59	1.24
zk2-1-1500-15	1228	3583	457	1802	353	58	287	236	133	111	2562	942	8248	9.8	0.56	1.23
zk2-1-1547-1	1357	3765	462	1740	307	67	235	179	93	77	428	398	8282	13.2	0.76	1.22
zk2-1-1547-2	1068	2908	352	1311	237	51	177	145	79	68	216	399	6396	12.6	0.76	1.22
zk2-1-1547-3	1748	4462	524	1922	333	69	250	192	108	91	253	597	9699	14.1	0.73	1.18
zk2-1-1547-4	1464	3782	449	1679	294	62	230	178	99	83	361	579	8320	13.1	0.73	1.18
zk2-1-1547-5	1924	5008	600	2204	391	73	292	221	121	97	1889	856	10931	14.0	0.66	1.19
zk2-1-1547-6	1326	3654	451	1687	312	64	228	174	92	72	1005	423	8060	13.2	0.73	1.22
zk2-1-1547-7	1288	3375	400	1468	257	56	194	147	83	68	331	342	7336	13.9	0.77	1.20
zk2-1-1547-8	1026	2698	345	1321	265	51	213	188	103	80	2659	744	6290	9.8	0.66	1.16
zk2-1-1547-9	1279	3345	392	1467	259	57	197	154	84	71	1662	595	7305	13.4	0.77	1.19
zk2-1-1547-10	1456	3783	446	1657	293	61	224	173	96	79	189	425	8268	13.5	0.73	1.19
zk2-1-1547-11	1405	3742	442	1577	266	63	194	140	75	59	589	255	7963	16.0	0.85	1.23
zk2-1-1547-12	1630	4191	487	1787	310	67	236	184	103	90	210	590	9085	13.8	0.76	1.19

Note: δ Eu = $(\text{Eu}/\text{Eu}^+)_N = \text{Eu}_N/\sqrt{\text{Sm}_N + \text{Gd}_N}$; δ Ce = $(\text{Ce}/\text{Ce}^+)_N = \text{Ce}_N/\sqrt{\text{La}_N + \text{Pr}_N}$; LREE = La + Ce + Pr + Nd + Sm; HREE = Gd + Dy + Er + Yb.

3.2. Analytical methods

Electron probe microanalysis (EPMA) and *in situ* laser ablation inductively coupled plasma mass spectrometry (LA-ICP-MS) were conducted at the University of Tasmania. Analytical conditions for the EPMA include: Voltage: 15 kV; Current: 20 nA; Beam size: 2 μm . Analytical accuracies for most elements were about 0.1%.

The LA-ICP-MS analysis was performed on an Agilent 7900 quadrupole ICP-MS coupled with a 193 nm Coherent Ar-F excimer laser and an ASI Resolution S155 ablation cell. The downhole fractionation, instrumental drift and mass bias correction factors for Pb/U ratios on

titanite were calculated using an in-house primary standard (100606 titanite) and secondary standard titanite (19686 titanite), which were analyzed at the beginning of the session and after every 12 unknown titanite determinations (roughly every 1/2 h). The correction factor for the $^{207}\text{Pb}/^{206}\text{Pb}$ ratio was calculated using two NIST610 analyses with the values recommended by Baker et al. (2004).

Each analysis on the titanite began with a 30 s blank gas measurement followed by a further 30 s of analysis time when the laser was switched on. Titanite was sampled with a 29 μm laser spot using the laser at 5 Hz and a fluence of approximately 2 J/cm². A flow of He carrier gas at a rate of 0.35 L/min carried particles ablated by the laser

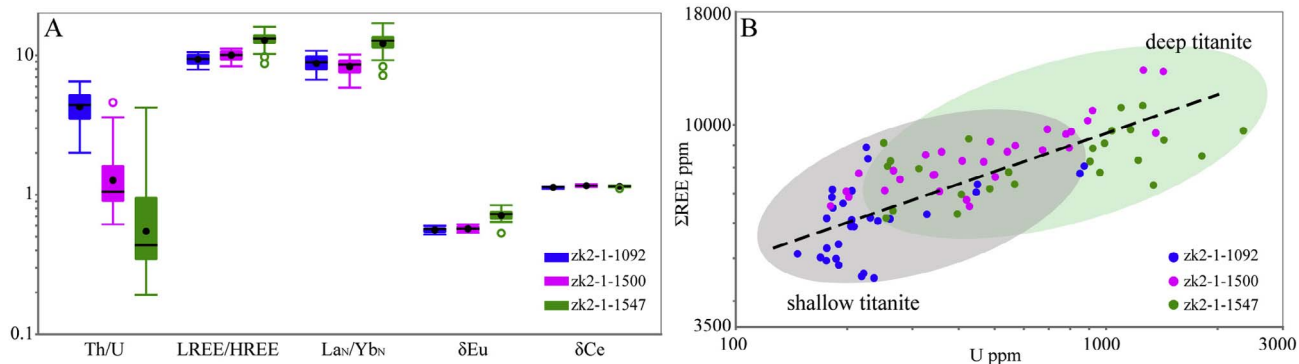


Fig. 4. (A) Box plot of Luohé titanite trace elements; (B) Binary U vs. Σ REE diagram.

out of the chamber to be mixed with Ar gas and carried to the plasma torch. Isotopes measured were ^{43}Ca , ^{49}Ti , ^{56}Fe , ^{90}Zr , ^{93}Nb , ^{139}La , ^{140}Ce , ^{141}Pr , ^{146}Nd , ^{147}Sm , ^{153}Eu , ^{157}Gd , ^{163}Dy , ^{166}Er , ^{172}Yb , ^{202}Hg , ^{204}Pb , ^{206}Pb , ^{207}Pb , ^{208}Pb , ^{232}Th and ^{238}U , with each element being measured every 0.17 s, with longer counting time on the Pb isotopes than the other isotopes. The data reduction used was based on the method outlined in detail in Halpin et al. (2014) with an additional modification to help correct for the small amount of common Pb present in the primary standard using the ^{207}Pb correction of Chew et al. (2014).

4. Results

4.1. Major and trace elements of titanite

The major and trace element analysis results are listed in Tables 1 and 2. The two deep titanite samples are geochemically similar in major elements: zk2-1-1500 contains $\text{SiO}_2 = 29.7\text{--}30.3\text{ wt\%}$; $\text{TiO}_2 = 33.9\text{--}36.0\text{ wt\%}$; $\text{CaO} = 27.1\text{--}27.9\text{ wt\%}$; $\text{Al}_2\text{O}_3 = 1.09\text{--}1.99\text{ wt\%}$; $\text{FeO} = 1.53\text{--}2.16\text{ wt\%}$ and $\text{F} = 0.56\text{--}1.03\text{ wt\%}$. zk2-1-1547 contains $\text{SiO}_2 = 29.7\text{--}30.6\text{ wt\%}$; $\text{TiO}_2 = 34.2\text{--}37.1\text{ wt\%}$; $\text{CaO} = 27.5\text{--}28.5\text{ wt\%}$; $\text{Al}_2\text{O}_3 = 0.94\text{--}2.1\text{ wt\%}$; $\text{FeO} = 1.33\text{--}2.12\text{ wt\%}$ and $\text{F} = 0.52\text{--}1.06\text{ wt\%}$. The shallow-level zk2-1-1092 contains $\text{SiO}_2 = 30.0\text{--}30.6\text{ wt\%}$; $\text{TiO}_2 = 34.9\text{--}41.0\text{ wt\%}$; $\text{CaO} = 25.0\text{--}28.3\text{ wt\%}$; $\text{Al}_2\text{O}_3 = 1.06\text{--}1.66\text{ wt\%}$; FeO (total Fe) = 1.53–2.20 wt% and $\text{F} = 0.57\text{--}0.85\text{ wt\%}$. The shallow-level titanite contains wider Ca-Ti concentration ranges, whereas the deep-level titanite contains wider Al and F concentration ranges. The Si-Fe concentration ranges are essentially the same for both shallow- and deep-level titanite.

Deep-level titanite contains higher total REE contents ($\Sigma\text{REE} = 6160\text{--}13282\text{ ppm}$, average 8491 ppm) and high chondrite-normalized LREE/HREE ratios (8.4–16.0, average 11.4; $(\text{La}/\text{Yb})_N = 5.9\text{--}17.0$, average at 10.2) (Fig. 4A), and shows distinct negative Eu anomalies ($\delta\text{Eu} = 0.53\text{--}0.84$) and weak positive Ce anomalies ($\delta\text{Ce} = 1.11\text{--}1.19$). Variation of Th (138–1355 ppm, average 520 ppm) and U (168–2347 ppm, average 676 ppm) concentrations and Th/U ratios (0.19–4.60) are large (Fig. 4A). Variations of U and Σ REE concentrations are to some extent consistent with each other (Fig. 4B).

The shallow-level titanite contains lower Σ REE (4511–8893 ppm, average 6222 ppm). Its LREE/HREE and $(\text{La}/\text{Yb})_N$ ratios are 7.9–10.5 (average 9.4) and 6.7–10.8 (average 8.8), respectively, indicating significant LREE/HREE fractionation. The mineral also contains distinct negative Eu anomalies ($\delta\text{Eu} = 0.52\text{--}0.60$) and weak positive Ce anomalies ($\delta\text{Ce} = 1.10\text{--}1.14$). Its Th and U concentrations are 716–1762 ppm (average 1037 ppm) and 147–873 ppm (average 266 ppm), respectively, yielding relatively high and variable Th/U ratios (2.00–6.47) (Fig. 4A). Again, U is positively correlated with total REE (Fig. 4B).

4.2. Titanite U-Pb ages

Some titanite grains in our samples contain slightly higher common Pb and varying Pb/U, and choosing an initial Pb isotopic composition to calculate the age may not be appropriate (Frost et al., 2001). Thus, we use the ^{207}Pb -correction method to calculate the titanite age (Stern, 1997; Aleinikoff et al., 2002). The uncorrected data are plotted in the Tera-Wasserburg diagram (Fig. 5), and these analyses yielded a lower intercept that approximates the titanite age. The y-intercept initial $^{207}\text{Pb}/^{206}\text{Pb}$ can be used to obtain the individual ^{207}Pb -corrected $^{206}\text{Pb}/^{238}\text{U}$ ages (Stern, 1997; Frost et al., 2001), which can be used to calculate the weighted average age of titanite. As shown in the Tera-Wasserburg concordia diagram, shallow-level sample zk2-1-1092 yielded a U-Pb intercept age of $130.0 \pm 0.9\text{ Ma}$, and a ^{207}Pb corrected $^{206}\text{Pb}/^{238}\text{U}$ weighted average age of $130.0 \pm 0.8\text{ Ma}$ ($n = 29$, MSWD = 1.7), consistent with the lower intercept age within analytical error (Fig. 5A, B).

Deep-level titanite sample zk2-1-1500 yielded a intercept age of $128.8 \pm 0.6\text{ Ma}$, and a ^{207}Pb corrected $^{206}\text{Pb}/^{238}\text{U}$ weighted average age of $129.1 \pm 0.8\text{ Ma}$ ($n = 21$, MSWD = 1.5) (Fig. 5C, D). Sample zk2-1-1547 yielded a U-Pb intercept age of $129.5 \pm 0.5\text{ Ma}$, and a ^{207}Pb corrected $^{206}\text{Pb}/^{238}\text{U}$ weighted average age of $129.7 \pm 0.8\text{ Ma}$ ($n = 21$, MSWD = 1.3), consistent with the lower intercept age within analytical error (Fig. 5E, F). The titanite grains have no obvious textural difference under the microscope (Fig. 6A), but analysis spots within a single titanite grain can have very different ages. BSE imaging also shows that the titanite composition is not homogenous (Fig. 6B, Table 3). The significantly younger U-Pb ages of the titanite were possibly formed by thermal resetting by younger intrusions, e.g., syenite dikes.

5. Discussion

5.1. Origin of the Luohé titanite

The Luohé titanite is largely euhedral to subhedral, and coexists with hydrothermal minerals (e.g., magnetite, diopside, anhydrite, epidote and apatite) in crosscutting veins, which indicates its hydrothermal origin. BSE imaging reveals no consistent zonation in the titanite (Fig. 3G, H), which suggests that the titanite was precipitated in one mineralizing event. Previous titanite geochemical studies (e.g., Cempírek et al., 2008; Horie et al., 2008; Olin and Wolff, 2012; Che et al., 2013; Cao et al., 2015) indicated negative TiO_2 vs. $(\text{FeO} + \text{Al}_2\text{O}_3)$ and TiO_2 vs. F correlations (Fig. 7A, B), which suggests the occurrence of the replacement reaction $[(\text{Al}, \text{Fe})^{3+} + (\text{F}, \text{OH})^- = \text{Ti}^{4+} + \text{O}^{2-}]$, which is promoted by high temperature ($> 500^\circ\text{C}$) and pressure (Tropper et al., 2002).

LA-ICP-MS titanite trace element data reveal that the Luohé titanite is enriched in Zr, Nb and REEs, with the $(\text{Zr} + \text{Nb} + \Sigma\text{REE})$

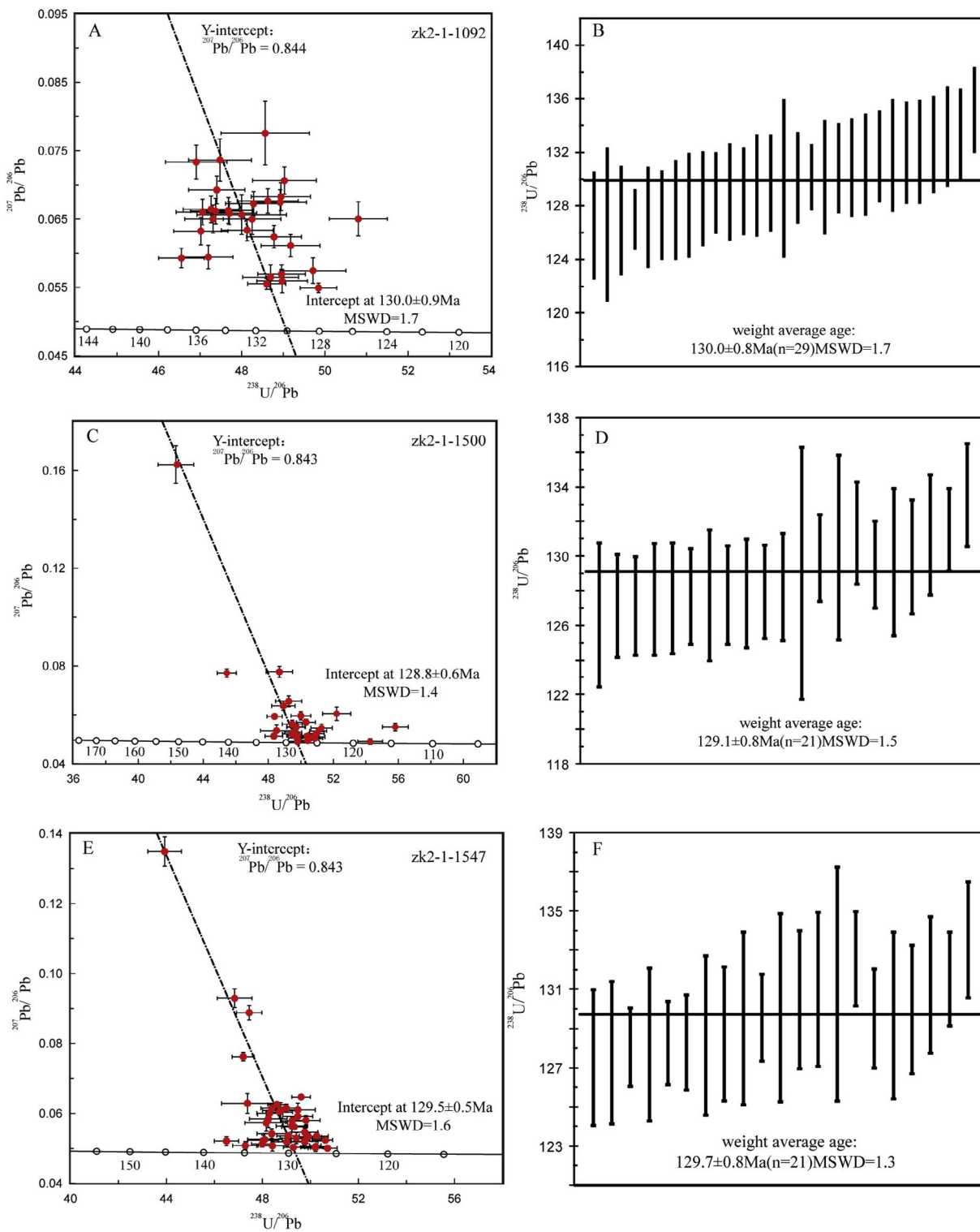


Fig. 5. LA-ICP-MS U-Pb diagrams (A, C, E) and weighted average age (B, D, F) for the Luohetitanite.

concentrations of the shallow- and deep-level titanite being 0.66–1.73% and 0.70–1.76%, respectively. Previous studies suggested that REEs would replace Ca in titanite crystal lattice, and HFSEs (e.g., Zr and Nb) would replace Ti (-Al-Fe) (Della Ventura et al., 1999). The positive Zr vs. Nb correlation for the Luohetitanite suggests their similar role in the replacement reaction (Fig. 7C). Zr can replace Ti in titanite, and the extent of replacement correlates positively with temperature (under similar pressure; Hayden et al., 2008). According to Einaudi et al.

(1981) and Hayden et al. (2008), typical skarn alteration can occur under 0.1–0.3 GPa, with $a\text{TiO}_2 = a\text{SiO}_2 = 0.5$. Titanite thermobarometric calculation (i.e., Zr-titanite (ppm) = $10.52(\pm 0.01)$ – $7708(\pm 101)/T(\text{K})$ – $960(\pm 10) * P(\text{GPa})/T(\text{K}) - \log(a\text{TiO}_2) - \log(a\text{SiO}_2)$) yielded formation temperatures for the Luohetitanite of 620–820 °C (average 730 °C, n = 86). Titanite from the Jinshidian Fe skarn deposit (which is located in the MLYB) has yielded formation temperatures of ca. 452–793 °C (Zhu et al., 2014). Some of the Jinshidian titanite coexists

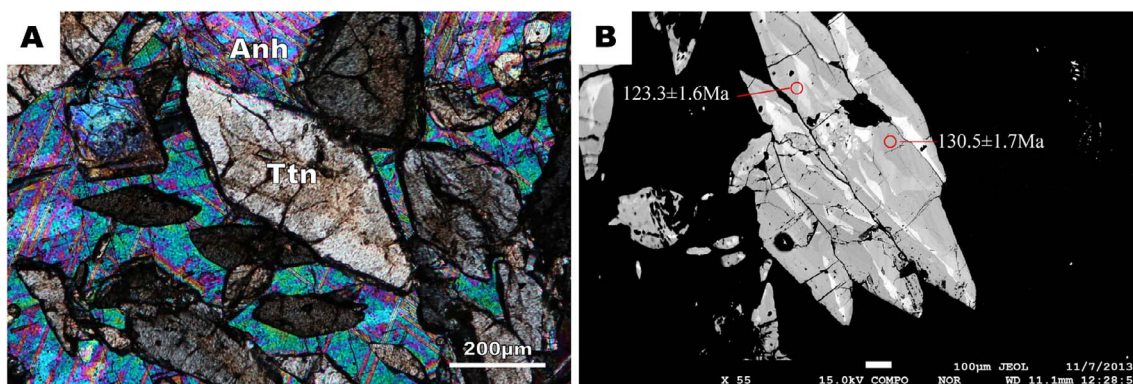


Fig. 6. (A) Photomicrograph of a deep-level titanite grain; (B) BSE image showing individual titanite grains have complex structure and different parts yield different ages.

with skarn minerals (diopside and garnet), and has formation temperature similar to Luohé, which coexists with magnetite. The association of the Luohé titanite with magnetite and large amounts of fluorapatite and phlogopite, suggest that the Luohé deposit formed in a high temperature, F-rich system, favorable for titanium migration.

Titanite Th/U ratios can be used as genetic indicators. In general, hydrothermal titanite contains lower Th/U (mostly < 1), whereas that of magmatic titanite is higher (Alekinoff et al., 2002; Gao et al., 2012; Che et al., 2013; Deng et al., 2015). The Luohé titanite contains a wide Th/U range (zk2-1-1092 = 2.0–6.5, average 4.4; zk2-1-1500 = 0.6–4.6, average 1.4; zk2-1-1547 = 0.2–4.2, average 0.7). Relatively high Th/U ratios were reported from the hydrothermal titanite in both the Tonglushan Cu-Au-Fe skarn deposit (SE Hubei province) (1.45–3.22; Li et al., 2010) and Jinshadian Fe skarn deposit (1.94–17.20; Zhu et al., 2014), and the Th/U ratios correlate positively with Zr concentrations (Fig. 7D). As mentioned before, titanite Zr concentrations increase with temperature, and the Th/U ratios also increase with temperature. Therefore, hydrothermal titanite crystallized at high temperature would also have $\text{Th}/\text{U} > 1$, suggesting that Th/U ratios could not clearly discriminate between titanite formed under high temperature magmatic/hydrothermal conditions, whether from skarn- or magnetite-apatite type deposits.

Titanite trace elements are indicative of its origin. Titanite from Fe (-Cu) skarn deposits could be formed at different stages of the hydrothermal alteration, and would display distinct mineral and geochemical characteristics (Li et al., 2010; Zhu et al., 2014). The Luohé hydrothermal titanite probably began to crystallize in the diopside-anhydrite alteration stage, and coexists with diopside, magnetite and apatite. The three Luohé titanite samples have similar REE compositions, including right-dipping REE patterns, and high ΣREE and distinct negative Eu anomalies. These features are also shared by the hydrothermal titanite (skarn stage) from the Jinshadian Fe skarn deposit (Fig. 8A, Zhu et al., 2014), suggesting that the two deposits may have a similar environment of formation and fluid source.

As for the other deposits in this area (e.g., Ruanjiawan and Tonglushan) (Li et al., 2010; Deng et al., 2015), hydrothermal titanite from the Ruanjiawan W-Mo-Cu skarn deposit contains lower ΣREE and shows LREE depletions. The depletion of LREEs in the altered titanite can be interpreted to result from the formation of LREE-enriched epidote during the hydrothermal alteration (Deng et al., 2015). The Tonglushan hydrothermal epidote-hosted titanite and calcite-hosted titanite have very different REE patterns (Li et al., 2010, Fig. 8B), which also indicate that the formation of LREE-enriched minerals (e.g., apatite and epidote) with decreasing temperature can deplete LREE in the residual fluids. The Luohé hydrothermal titanite REE patterns are similar to those of typical magmatic titanite (Fig. 8A, B), indicating that the titanite may have formed earlier than the LREE-rich minerals, and that the titanite REE compositions are not significantly changed by later

fluid alteration. Europium anomalies of titanite are mainly influenced by oxygen fugacity ($f\text{O}_2$): Oxidation of Eu^{2+} into Eu^{3+} would inhibit its replacement for Ca^{2+} in the titanite crystal lattice, creating the distinct negative Eu anomalies (Horie et al., 2008). In this study, samples zk2-1-1092 and zk2-1-1500 show distinct negative Eu anomalies, whereas that of zk2-1-1547 is much less distinctive (Fig. 8C), which shows increasing $f\text{O}_2$ during fluid ascent and/or migration from deep to shallow.

5.2. Age of the Luohé Fe deposit

No obvious core-rim texture was found in the Luohé titanite by either microscopic petrography or BSE imaging (except patchy textures in very few titanite grains), suggesting a single-phase hydrothermal crystallization. The coexistence of titanite with magnetite (Fig. 3A, B) suggests that the titanite U-Pb age reflects also the Fe mineralization age. In this study, the shallow-level Luohé hydrothermal titanite yielded a ^{207}Pb -corrected $^{206}\text{Pb}/^{238}\text{U}$ weighted average age of 130.0 ± 0.8 Ma, whilst the two deep-level Luohé hydrothermal titanite samples yielded weighted average ages of 129.1 ± 0.8 Ma– 129.7 ± 0.8 Ma. This indicates that the two deep-level titanite samples have similar ages (within analytical error). The consistent ages (ca. 130 Ma; within analytical error) and REE distribution patterns of the three Luohé titanite samples suggest that the ore fluids in the shallow- and deep-level orebodies may have had the same magmatic-hydrothermal source and belong to the same hydrothermal system. Combined with ore geological features, we propose that the shallow- and deep-level orebodies at Luohé were deposited from the same mineralizing system.

There are over 30 intrusions (ca. $0.1\text{--}50\text{ km}^2$ each) in the Lu-Zong mineral district. Previous geochronological studies on these intrusions (Fan et al., 2008, 2014a,b; Zhou et al., 2007, 2010a,b; Zhang, 2011; Qiu, 2014) have placed these intrusions into three major phases: (1) 134–132 Ma buried diorite that is closely related to the Fe mineralization; (2) 134–130 Ma monzonite and syenite in northern Lu-Zong; (3) 129–123 Ma quartz syenite and A-type granite in southern Lu-Zong. The age of the Luohé magnetite mineralization (ca. 130 Ma) is consistent with either the first or second intrusive phases, yet field investigation found that the second-phase syenite crosscuts the orebodies, suggesting that the Luohé ore-forming magmas may have been diorite of the first intrusive phase.

6. Conclusions

- (1) Formation temperatures of the Luohé titanite from the shallow- and deep-level orebodies were calculated to be similar (ca. 700°C); this is believed to be the magnetite deposition temperature, and is higher than mineralization temperature of typical Fe skarn deposits.
- (2) The Luohé hydrothermal titanite shows LREE-enrichment (which is typical of igneous titanite), and its crystallization was probably

Table 3

LA-ICP MS U-Th-Pb isotope data for titanite grains.

Analysis number	Concentration (ppm)			Th/U	Measured isotopic ratios						$^{206}\text{Pb}/^{238}\text{U}$ (Ma)		^{207}Pb -Corrected ages (Ma)			
	Th	U	Pb		$^{238}\text{U}/^{206}\text{Pb}$	$^{206}\text{Pb}/^{238}\text{U}$	1σ	$^{208}\text{Pb}/^{232}\text{Th}$	1σ	$^{207}\text{Pb}/^{206}\text{Pb}$	1σ	Age	1σ	$^{206}\text{Pb}/^{238}\text{U}$	1σ	
Shallow	ZK2-1-1092-1	1762	873	27.7	2.02	49.75	0.0201	0.0088	0.0065	0.014	0.0549	0.0124	128.05	1.13	127.03	1.12
	ZK2-1-1092-2	1040	242	11.1	4.3	49.02	0.0204	0.0145	0.0067	0.0172	0.0683	0.03	130.39	1.90	127.19	1.87
	ZK2-1-1092-3	797	190	8.7	4.2	49.02	0.0204	0.0129	0.0067	0.0156	0.0675	0.0274	130.43	1.68	127.37	1.66
	ZK2-1-1092-4	929	209	9.8	4.45	49.26	0.0203	0.0144	0.0067	0.0157	0.0611	0.0269	129.78	1.87	127.75	1.85
	ZK2-1-1092-5	759	187	8.3	4.07	48.54	0.0206	0.0151	0.0065	0.0161	0.0676	0.0263	131.22	1.98	128.11	1.94
	ZK2-1-1092-6	781	221	9.3	3.52	48.78	0.0205	0.0136	0.0068	0.016	0.0624	0.0261	130.83	1.77	128.58	1.75
	ZK2-1-1092-7	1287	449	16.5	2.86	49.02	0.0204	0.0116	0.0066	0.0151	0.0569	0.0236	130.35	1.52	129	1.51
	ZK2-1-1092-8	1325	205	12.2	6.47	48.31	0.0207	0.0139	0.0067	0.0145	0.0673	0.0262	132.14	1.84	129.08	1.81
	ZK2-1-1092-9	1353	228	12.7	5.95	49.02	0.0204	0.0124	0.0066	0.0151	0.0559	0.0304	130.31	1.62	129.12	1.62
	ZK2-1-1092-10	760	176	8.4	4.33	48.31	0.0207	0.0144	0.0068	0.0157	0.065	0.0346	132.24	1.90	129.55	1.89
	ZK2-1-1092-11	1071	225	10.9	4.76	48.78	0.0205	0.0138	0.0065	0.0153	0.0565	0.0315	131.05	1.81	129.76	1.8
	ZK2-1-1092-12	758	219	8.5	3.47	48.08	0.0208	0.0224	0.0065	0.0215	0.0656	0.044	132.92	2.98	130.11	2.94
	ZK2-1-1092-13	1104	200	10.6	5.51	48.08	0.0208	0.013	0.0064	0.015	0.0634	0.0244	132.56	1.72	130.13	1.7
	ZK2-1-1092-14	1703	850	27.5	2	48.54	0.0206	0.0094	0.0067	0.0144	0.0555	0.0145	131.29	1.24	130.17	1.22
	ZK2-1-1092-15	1081	206	10.6	5.25	47.39	0.0211	0.0159	0.0067	0.0177	0.0736	0.042	134.37	2.14	130.19	2.12
	ZK2-1-1092-16	984	206	10.3	4.78	47.62	0.0210	0.0125	0.0068	0.015	0.0663	0.0285	133.80	1.68	130.87	1.66
	ZK2-1-1092-17	830	189	9.0	4.38	47.62	0.0210	0.0138	0.0066	0.0155	0.0659	0.0255	133.75	1.85	130.88	1.82
	ZK2-1-1092-18	943	183	9.6	5.16	47.39	0.0211	0.0143	0.0067	0.0154	0.0693	0.0295	134.59	1.92	131.13	1.89
	ZK2-1-1092-19	1044	231	11.2	4.52	47.39	0.0211	0.0128	0.0067	0.0156	0.0662	0.028	134.66	1.72	131.73	1.7
	ZK2-1-1092-20	716	147	7.6	4.88	46.95	0.0213	0.0157	0.0068	0.0155	0.0733	0.0341	135.99	2.14	131.81	2.1
	ZK2-1-1092-21	823	176	8.8	4.67	47.17	0.0212	0.0142	0.0068	0.0162	0.0664	0.0292	134.97	1.92	131.99	1.89
	ZK2-1-1092-22	737	169	8.2	4.36	47.39	0.0211	0.0144	0.0069	0.0162	0.065	0.0314	134.84	1.94	132.1	1.92
	ZK2-1-1092-23	1111	182	10.7	6.11	46.95	0.0213	0.0135	0.0068	0.0147	0.066	0.0287	135.55	1.83	132.63	1.81
	ZK2-1-1092-24	924	182	9.4	5.06	46.95	0.0213	0.0139	0.0066	0.0156	0.0632	0.0317	135.67	1.88	133.22	1.87
	ZK2-1-1092-25	1341	446	16.6	3.01	47.17	0.0212	0.0126	0.0068	0.0172	0.0594	0.0288	135.16	1.70	133.36	1.69
	ZK2-1-1092-26	1109	328	13.9	3.38	46.51	0.0215	0.0118	0.0068	0.0146	0.0593	0.024	137.02	1.61	135.22	1.60
	ZK2-1-1092-27	1038	176	9.7	5.90	49.03	0.0204	0.0156	0.0067	0.0152	0.0706	0.0282	130.17	2.04	126.59	1.99
	ZK2-1-1092-28	1117	195	11.0	5.73	48.56	0.0206	0.0219	0.0065	0.0228	0.0776	0.0600	131.39	2.88	126.65	2.86
	ZK2-1-1092-29	777	236	9.2	3.29	49.71	0.0201	0.0159	0.0065	0.0186	0.0574	0.0327	128.38	2.04	126.97	2.03
Deep	ZK2-1-1500-1	829	180	8.6	4.6	49.26	0.0203	0.0163	0.0066	0.017	0.0656	0.0334	129.36	2.11	126.62	2.08
	ZK2-1-1500-2	364	428	10.6	0.85	49.75	0.0201	0.0116	0.0069	0.0192	0.055	0.0223	128.19	1.49	127.16	1.48
	ZK2-1-1500-3	518	278	8.6	1.87	49.75	0.0201	0.0111	0.0066	0.018	0.0551	0.025	128.21	1.43	127.17	1.42
	ZK2-1-1500-4	585	674	16.4	0.87	49.75	0.0201	0.0126	0.0066	0.0227	0.0516	0.031	128.00	1.61	127.53	1.61
	ZK2-1-1500-5	307	253	6.9	1.22	49.50	0.0202	0.0124	0.0072	0.0197	0.0562	0.0286	128.80	1.60	127.58	1.6
	ZK2-1-1500-6	458	502	12.3	0.91	49.75	0.0201	0.0108	0.0066	0.0196	0.0506	0.0227	128.01	1.38	127.7	1.38
	ZK2-1-1500-7	552	215	7.7	2.57	49.02	0.0204	0.0146	0.0066	0.0182	0.0637	0.0295	130.21	1.91	127.76	1.88
	ZK2-1-1500-8	485	487	12.5	1	49.75	0.0201	0.0111	0.0065	0.0217	0.0515	0.0271	128.26	1.42	127.79	1.43
	ZK2-1-1500-9	837	1362	31.1	0.61	50.00	0.0200	0.0123	0.0066	0.0227	0.0491	0.0223	127.95	1.58	127.87	1.57
	ZK2-1-1500-10	494	359	10.0	1.37	49.50	0.0202	0.0105	0.0066	0.0177	0.0529	0.0245	128.65	1.35	127.96	1.35
	ZK2-1-1500-11	409	409	10.6	1	49.50	0.0202	0.012	0.007	0.0197	0.0522	0.0234	128.81	1.55	128.24	1.54
	ZK2-1-1500-12	570	326	19.8	1.75	42.37	0.0236	0.026	0.0104	0.0353	0.1624	0.0476	150.29	3.90	129.05	3.64
	ZK2-1-1500-13	625	568	15.4	1.1	48.54	0.0206	0.0096	0.0072	0.0165	0.0593	0.0165	131.67	1.27	129.91	1.25
	ZK2-1-1500-14	492	344	10.8	1.43	48.54	0.0206	0.0204	0.0064	0.0312	0.0536	0.0425	131.33	2.68	130.52	2.67
	ZK2-1-1500-15	734	467	14.1	1.57	48.31	0.0207	0.0112	0.0068	0.0167	0.0513	0.0223	131.78	1.48	131.35	1.47
	ZK2-1-1500-16	626	202	10.2	3.1	47.62	0.0210	0.0097	0.0086	0.0202	0.0762	0.016	134.14	1.30	129.54	1.26
	ZK2-1-1500-17	626	267	13.7	2.35	48.54	0.0206	0.0162	0.0079	0.0372	0.0584	0.0424	131.28	2.12	129.68	2.12
	ZK2-1-1500-18	1032	694	8.2	1.49	48.78	0.0205	0.0126	0.0058	0.0168	0.0542	0.026	130.90	1.65	129.99	1.64
	ZK2-1-1500-19	535	795	20.2	0.67	48.31	0.0207	0.0132	0.0064	0.0322	0.0523	0.0289	131.85	1.74	131.25	1.74
	ZK2-1-1500-20	787	805	32.0	0.98	48.31	0.0207	0.0091	0.006	0.02	0.0512	0.0161	131.97	1.20	131.55	1.2
	ZK2-1-1500-21	324	420	11.0	0.77	47.62	0.0210	0.0111	0.0063	0.0228	0.0508	0.022	133.89	1.49	133.55	1.48
	ZK2-1-1547-1	255	262	7.6	0.97	49.75	0.0201	0.0135	0.0068	0.0234	0.053	0.0298	128.24	1.73	127.54	1.73
	ZK2-1-1547-2	213	266	12.7	0.8	48.78	0.0205	0.014	0.0073	0.0274	0.0678	0.0312	130.93	1.83	127.79	1.81
	ZK2-1-1547-3	450	2347	10.9	0.19	49.02	0.0204	0.0077	0.0101	0.019	0.0625	0.0114	130.33	1.01	128.07	0.99
	ZK2-1-1547-4	94	139	22.0	0.68	48.54	0.0206	0.0149	0.0085	0.0308	0.0682	0.0377	131.40	1.96	128.2	1.94
	ZK2-1-1547-5	382	1221	31.0	0.31	49.75	0.0201	0.0084	0.0067	0.019	0.0503	0.0125	128.56	1.07	128.28	1.07
	ZK2-1-1547-6	459	1097	7.1	0.42	49.50	0.0202	0.0095	0.0069	0.0201	0.0536	0.014	129.12	1.22	128.31	1.22
	ZK2-1-1547-7	244	257	21.9	0.95	46.95	0.0213	0.0155	0.0087	0.0246	0.0929	0.029	136.18	2.11	128.67	2.03
	ZK2-1-1547-8	243	566	22.1	0.43	49.26	0.0203	0.0132	0.0066	0.0343	0.0519	0.0303	129.27	1.71</		

Table 3 (continued)

Analysis number	Concentration (ppm)			Th/U	Measured isotopic ratios						$^{206}\text{Pb}/^{238}\text{U}$ (Ma)		^{207}Pb -Corrected ages (Ma)			
	Th	U	Pb		$^{238}\text{U}/^{206}\text{Pb}$	$^{206}\text{Pb}/^{238}\text{U}$	1σ	$^{208}\text{Pb}/^{232}\text{Th}$	1σ	$^{207}\text{Pb}/^{206}\text{Pb}$	1σ	Age	1σ	$^{206}\text{Pb}/^{238}\text{U}$	1σ	
Younger sp-ots	ZK2-1-1500	626	202	21.0	3.1	52.36	0.0191	0.0166	0.0065	0.0209	0.0605	0.0028	122.13	2.03	120.29	2.03
	ZK2-1-1500	626	267	22.2	2.35	51.28	0.0195	0.0128	0.0067	0.0185	0.0546	0.0016	124.32	1.60	123.36	1.59
	ZK2-1-1500	1032	694	7.6	1.49	51.02	0.0196	0.0101	0.0065	0.015	0.0534	0.0009	124.82	1.27	124.05	1.25
	ZK2-1-1547	195	485	10.4	0.4	52.91	0.0189	0.0161	0.0072	0.0369	0.0521	0.0344	120.69	1.94	120.13	1.94
	ZK2-1-1547	405	426	10.4	0.95	52.08	0.0192	0.0114	0.0061	0.0225	0.0528	0.0255	122.48	1.40	121.81	1.4
	ZK2-1-1547	439	1255	28.0	0.35	51.55	0.0194	0.0106	0.008	0.0232	0.061	0.0186	124.06	1.32	122.12	1.3
	ZK2-1-1547	525	1164	33.8	0.45	49.50	0.0202	0.0112	0.0101	0.0302	0.0856	0.0282	129.14	1.45	123.17	1.43
Primary Standard	19686-Titanite					0.1926	0.0123	0.0596	0.0227	0.0792	0.0189		1133.55		13.61	
	19686-Titanite					0.1933	0.0111	0.0567	0.0243	0.0796	0.0182		1137.05		12.26	
	19686-Titanite					0.1940	0.0108	0.0596	0.0217	0.0791	0.0171		1141.40		12.00	
	19686-Titanite					0.1940	0.0102	0.0600	0.0214	0.0781	0.0162		1142.80		11.30	
	19686-Titanite					0.1948	0.0107	0.0612	0.0217	0.0779	0.0143		1147.49		11.96	
	19686-Titanite					0.1950	0.0100	0.0587	0.0213	0.0785	0.0152		1147.83		11.19	
	19686-Titanite					0.1955	0.0103	0.0602	0.0218	0.0797	0.0169		1149.35		11.57	
	19686-Titanite					0.1956	0.0110	0.0583	0.0226	0.0798	0.0154		1149.53		12.29	
	19686-Titanite					0.1957	0.0108	0.0587	0.0199	0.0770	0.0160		1153.84		12.06	
	19686-Titanite					0.1964	0.0103	0.0582	0.0209	0.0793	0.0153		1154.53		11.53	
	19686-Titanite					0.1962	0.0105	0.0613	0.0211	0.0775	0.0127		1156.08		11.76	
Secondary Standard	100606					0.0732	0.0155	0.0252	0.0184	0.1069	0.0299		427.48		6.75	
	100606					0.0741	0.0141	0.0253	0.0190	0.1131	0.0280		429.01		6.22	
	100606					0.0744	0.0181	0.0264	0.0178	0.1153	0.0272		429.42		7.81	
	100606					0.0734	0.0125	0.0241	0.0158	0.1026	0.0230		431.03		5.44	
	100606					0.0751	0.0154	0.0259	0.0178	0.1145	0.0214		433.87		6.70	
	100606					0.0782	0.0176	0.0269	0.0206	0.1376	0.0315		438.28		8.00	
	100606					0.0764	0.0205	0.0261	0.0193	0.1065	0.0340		446.01		9.20	
	100606					0.0774	0.0140	0.0256	0.0168	0.1088	0.0257		450.28		6.40	
	100606					0.0762	0.0105	0.0246	0.0135	0.0927	0.0165		452.70		4.73	

- before or synchronous with the LREE-rich apatite and epidote.
- (3) Th/U ratios cannot effectively discriminate igneous vs. hydrothermal origin for high-temperature titanite.
 - (4) Luohé ore formation was dated at 130 Ma, coeval with widespread buried diorite intrusions in the basin, suggests that the Fe ore-forming fluids may have been derived from the diorite.

Acknowledgements

We thank Zhang Qianming and Gao Changsheng from the 327 Geological Brigade of Anhui Geology and Mineral Resources Exploration Bureau for their valuable support during the fieldwork. And thank Jay Thompson from Centre of Excellence in Ore Deposits for his

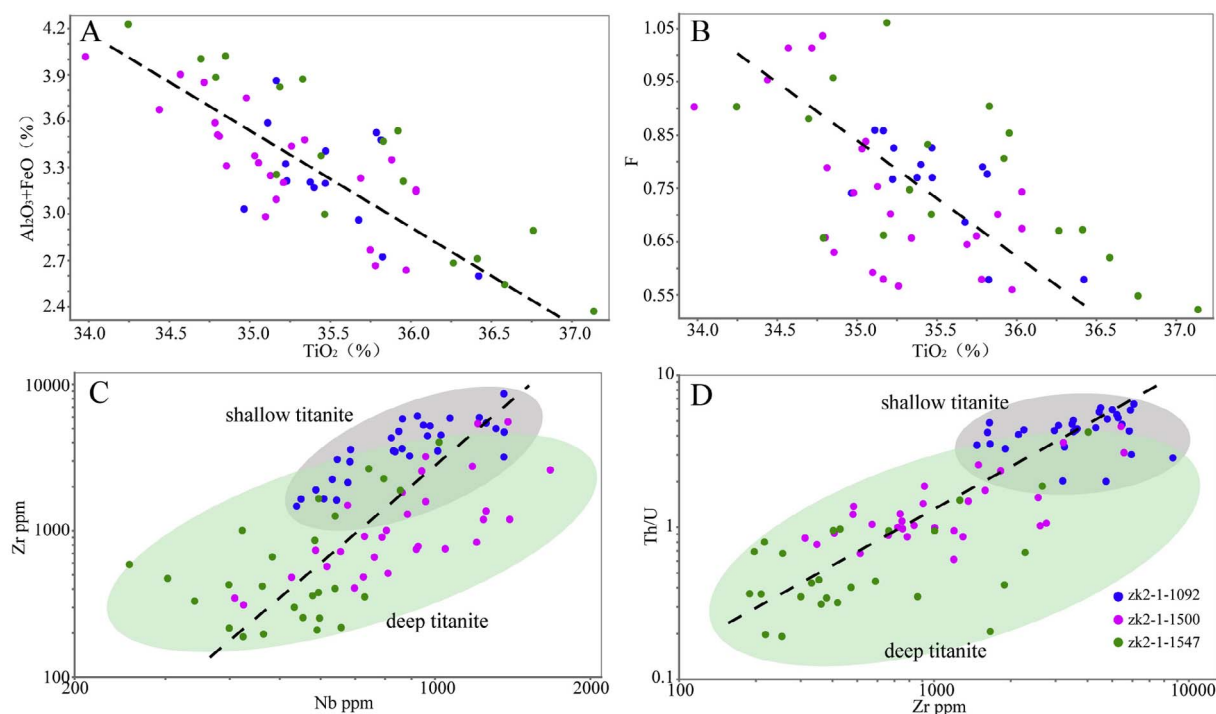


Fig. 7. (A) Al_2O_3 vs. TiO_2 ; (B) F vs. TiO_2 ; (C) Zr vs. Nb; (D) Th/U vs. Zr for the Luohé titanite.

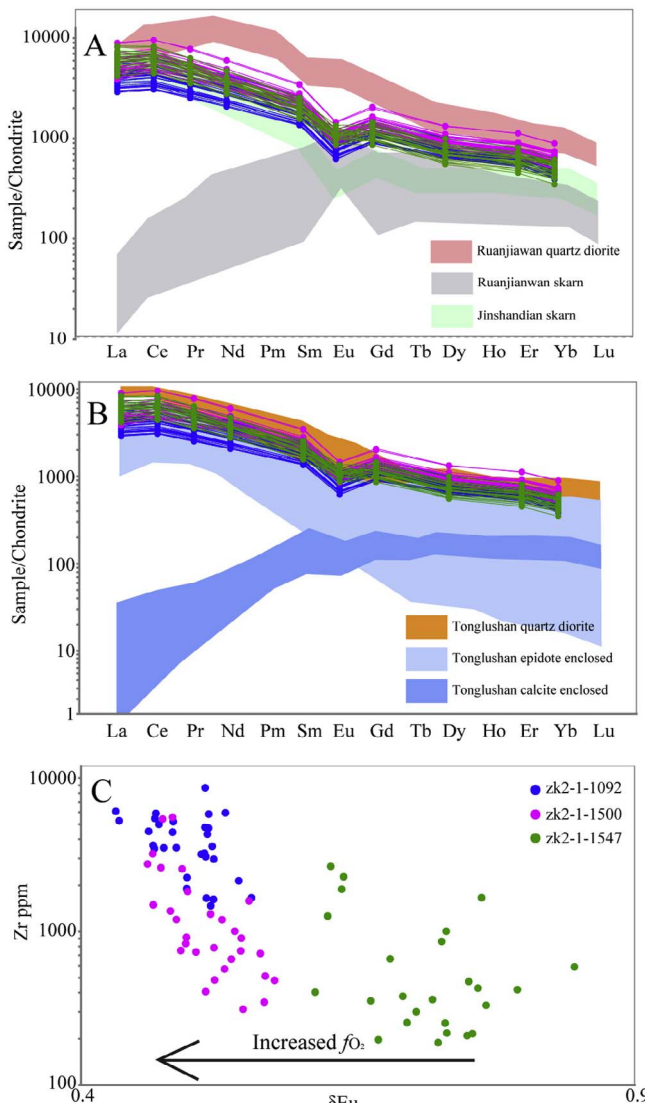


Fig. 8. (A and B) Chondrite-normalized REE patterns of titanite grains from Luohe deposit. The green area shows the REE compositions of titanite grains from the Jinshandian skarn Fe deposit (Zhu et al., 2014). The red and gray areas show the REE compositions of titanite grains from Ruanjiawan quartz diorite and mineralized skarn respectively (Deng et al., 2015). The orange and blue areas show the REE compositions of titanite grains from the Tonglushan deposit (Li et al., 2010); (C) Zr vs. δ_{Eu} diagram for Luohe titanite. (For interpretation of the references to colour in this figure legend, the reader is referred to the web version of this article.)

help in the analysis. This work was financially supported by National Key Research and Development Plan (grant No. 2016YFC0600206), National Natural Science Foundation of China (grant Nos. 41672081, 41320104003, 41172084), and Public Welfare Project of Anhui Province (grant No. 2015-K-2, K-3).

References

- Aleinikoff, J.N., Wintsch, R.P., Fanning, C.M., Dorais, M.J., 2002. U-Pb geochronology of zircon and polygenetic titanite from the Glastonbury Complex, Connecticut, USA: an integrated SEM, EMPA, TIMS, and SHRIMP study. *Chem. Geol.* 188 (1), 125–147.
- Bonamici, C.E., Fanning, C.M., Kozdon, R., Fournelle, J.H., Valley, J.W., 2015. Combined oxygen-isotope and U-Pb zoning studies of titanite: new criteria for age preservation. *Chem. Geol.* 398, 70–84.
- Baker, J., Peate, D., Wright, T., Meyzen, C., 2004. Pb isotopic analysis of standards and samples using a Pb-207-Pb-204 double spike and thallium to correct for mass bias with a double-focusing MC-ICP-MS. *Chem. Geol.* 211, 275–303.
- Cao, M.J., Qin, K.Z., Li, G.M., Evans, N.J., Jin, L.Y., 2015. In situ LA-(MC)-ICP-MS trace element and Nd isotopic compositions and genesis of polygenetic titanite from the Baogutu reduced porphyry Cu deposit, Western Junggar, NW China. *Ore Geol. Rev.* 65, 940–954.
- Cemperek, J., Houzar, S., Novák, M., 2008. Complexly zoned niobian titanite from heedenbergite skarn at Písek, Czech Republic, constrained by substitutions Al(Nb, Ta)Ti₂, Al(F, OH)(TiO)₁ and SnTi-1. *Mineral. Mag.* 72 (6), 1293–1305.
- Chang, Y.F., Liu, X.P., Wu, Y.C., 1991. The Copper Iron Belt of the Lower and Middle Reaches of the Changjiang River. Geological Publishing House, Beijing, pp. 71–76 (in Chinese).
- Che, X.D., Linnen, R.L., Wang, R.C., Groat, L.A., Brand, A.A., 2013. Distribution of trace and rare earth elements in titanite from tungsten and molybdenum deposits in Yukon and British Columbia, Canada. *Can. Mineral.* 51 (3), 415–438.
- Chelle-Michou, C., Chiaradia, M., Selby, D., Ovtcharova, M., Spikings, R.A., 2015. High-resolution geochronology of the Corocochuayco porphyry-skarn deposit, Peru: a rapid product of the Incaic orogeny. *Econ. Geol.* 110, 423–443.
- Chiaradia, M., Vallance, J., Fontbote, L., Stein, H., Schaltegger, U., Coder, J., Richards, J., Villeneuve, M., Gendall, I., 2009. U-Pb, Re-Os, and 40Ar/39Ar geochronology of the Nambija Au-skarn and Pangui porphyry Cu deposits, Ecuador: implications for the Jurassic metallogenic belt of the Northern Andes. *Miner. Deposita* 44 (4), 371–387.
- Chew, D.M., Petrus, J.A., Kamber, B.S., 2014. U-Pb LA-ICPMS dating using accessory mineral standards with variable common Pb. *Chem. Geol.* 363, 185–199.
- Corfu, F., Grunsky, E.C., 1988. Igneous and tectonic evolution of the Batchawana greenstone belt, Superior Province: a U-Pb zircon and titanite study. *J. Geol.* 95 (1), 87–105.
- Della Ventura, G., Bellatreccia, F., Williams, C.T., 1999. Zr- and LREE-rich titanite from Tre Croci, Vico Volcanic complex (Latium, Italy). *Mineral. Mag.* 63 (1), 123–130.
- Deng, X.D., Li, J.W., Zhou, M.F., Zhao, X.F., Yan, D.R., 2015. In-situ LA-ICPMS trace elements and U-Pb analysis of titanite from the Mesozoic Ruanjiawan W-Cu-Moskarn deposit, Daye district, China. *Ore Geol. Rev.* 65, 990–1004.
- Dodson, M.H., 1973. Closure temperature in cooling geochronological and petrological systems. *Contrib. Miner. Petro.* 40, 259–274.
- Dong, S.W., Xiang, H.S., Gao, R., Liu, Q.T., Li, J.S., Zhan, S.Q., Lu, Z.W., Ma, L.C., 2010. Deep structure and ore formation within Lujiang-Zongyang volcanic ore concentrated area in Middle to Lower Reaches of Yangtze River. *Acta Petrol. Sinica* 26 (9), 2529–2542 (in Chinese with English abstract).
- Einaudi, M.T., Meinert, L.D., Newberry, R.J., 1981. Skarn deposits. *Econ. Geol.* 75th Anniversary Volume, 317–391.
- Fallourd, S., Poujol, M., Boulvais, P., Paquette, J.L., Blanquat, M.S., Remy, P., 2014. In situ LA-ICP-MS U-Pb titanite dating of Na-Ca metasomatism in orogenic belts: the North Pyrenean example. *Int. J. Earth Sci.* 103 (3), 667–682.
- Fan, Y., Liu, Y.N., Zhou, T.F., Zhang, L.J., Yuan, F., Wang, W.C., 2014a. Geochronology of the Nihe deposit and in the Lu-Zong basin and its metallogenetic significances. *Acta Petrol. Sinica* 30 (5), 1369–1381 (in Chinese with English abstract).
- Fan, Y., Qiu, H., Zhou, T.F., Yuan, F., Zhang, L.J., 2014b. LA-ICP-MS zircon U-Pb dating for the hidden intrusions in the Lu-Zong basin and its tectonic significance. *Acta Geol. Sinica* 88 (4), 532–546 (in Chinese with English abstract).
- Fan, Y., Zhou, T.F., Yuan, F., Qian, C.C., Lu, S.M., Cook, D., 2008. LA-ICP-MS zircon U-Pb ages of the A-type granites in the Lu-Zong (Lujiang-Zongyang) area and their geological significances. *Acta Petrol. Sinica* 24 (8), 1715–1724 (in Chinese).
- Frost, B.R., Chamberlain, K.R., Schumacher, J.C., 2001. Sphene (titanite): phase relations and role as a geochronometer. *Chem. Geo.* 172 (1–2), 131–148.
- Fu, Y., Sun, X.M., Zhou, H.Y., Lin, H., Yang, Y.J., 2016. In-situ LA-ICP-MS U-Pb geochronology and trace elements analysis of polygenetic titanite from the giant Beiya gold-polymetallic deposit in Yunnan Province Southwest China. *Ore Geol. Rev.* 77, 43–56.
- Gao, C.S., Zhang, Q.M., Shang, S.G., 2013. Census Geological Report of Xiaobaozhuang Iron Deposit in Lujiang Anhui Province. 327 Geological Team of Bureau of Geology and Mineral Resources Exploration, Hefei, Anhui province, pp. 42–65 (in Chinese).
- Gao, X.Y., Zheng, Y.F., Chen, Y.X., Guo, J.L., 2012. Geochemical and U-Pb age constraints on the occurrence of polygenetic titanites in UHP metagranite in the Dabie orogen. *Lithos* 136–139, 93–108.
- Giletti, B.J., Tullis, J., 1977. Studies in diffusion: pressure dependence of Ar diffusion in phlogopite mica. *Earth Planet. Sci. Lett.* 35, 180–183.
- Hayden, L.A., Watson, E.B., Wark, D.A., 2008. A thermobarometer for sphene (titanite). *Contrib. Miner. Petro.* 155 (4), 529–540.
- Halpin, J.A., Jensen, T., McGoldrick, P., Meffre, S., Berry, R.F., Everard, J.L., Calver, C.R., Thompson, J., Goemann, K., Whittaker, J.M., 2014. Authigenic monazite and detrital zircon dating from the Proterozoic Rocky Cape Group, Tasmania: links to the Belt-Purcell supergroup, North America. *Precambrian Res.* 250, 50–67.
- Horie, K., Hidaka, H., Gauthier-Lafaye, F., 2008. Elemental distribution in apatite, titanite and zircon during hydrothermal alteration: durability of immobilization mineral phases for actinides. *Phys. Chem. Earth*. 33, 962–968.
- Huang, Q.T., 1989. Luohe Iron Deposit in Anhui Province. Geological Publishing House, Beijing, pp. 1–209 (in Chinese).
- Ismail, R., Ciobanu, C.L., Cook, N.J., Teale, G.S., Giles, D., Mumm, A.S., Wade, B., 2014. Rare earths and other trace elements in minerals from skarn assemblages, Hillsides iron oxide-copper-gold deposit, Yorke Peninsula, South Australia. *Lithos* 184–187, 456–477.
- Kohn, M.J., Corrie, S.L., 2011. Preserved Zr-temperatures and U-Pb ages in high-grade metamorphic titanite: evidence for a static hot channel in the Himalayan orogen. *Earth Planet. Sci. Lett.* 311 (1–2), 136–143.
- Li, J.W., Deng, X.D., Zhou, M.F., Liu, Y.S., Zhao, X.F., Guo, J.L., 2010. Laser ablation ICP-MS titanite U-Th-Pb dating of hydrothermal ore deposits: a case study of the Tonglushan Cu-Fe-Au skarn deposit, SE Hubei Province, China. *Chem. Geol.* 270, 56–67.
- Liu, H., Qiu, J.S., Luo, Q.H., Xu, X.S., Ling, W.L., Wang, D.Z., 2002. Petrogenesis of the

- Mesozoic potash-rich volcanic rocks in the Lu-Zong basin, Anhui Province: geochemical constraints. *Geochemistry* 31 (2), 129–140.
- Liu, Y.N., 2015. Mineralization of Luohe-Xiaobaozhuang Iron Deposit in the Lu-Zong Volcanic Basin, Anhui Province (Master thesis). Hefei University of Technology, pp. 50–56.
- Liu, Y.N., Fan, Y., Gao, C.S., Zhang, Q.M., Zhang, L.J., 2016. Geological characteristics of Xiaobaozhuang iron deposit in the Lu-Zong volcanic basin, the Middle-Lower Yangtze River Valley Metallogenic Belt. *Acta Petrol. Sinica* 32 (2), 319–333 (in Chinese with English abstract).
- Mao, J.W., Wang, Y.T., Lehmann, B., Yu, J.J., Du, A.D., Mei, Y.X., Li, Y.F., Zang, W.S., Stein, H.J., Zhou, T.F., 2006. Molybdenite Re-Os and albite $^{40}\text{Ar}/^{39}\text{Ar}$ dating of Cu-Au-Mo and magnetite porphyry systems in the Yangtze River valley and metallogenic implications. *Ore Geol. Rev.* 29 (3–4), 307–324.
- Mazdab, F.K., 2009. Characterization of flux-grown trace-element-doped titanite using the high-mass-resolution ion microprobe (SHRIMP-RG). *Can. Mineral.* 47 (4), 813–831.
- Olin, P.H., Wolff, J.A., 2012. Partitioning of rare earth and high field strength elements between titanite and phonolitic liquid. *Lithos* 128–131, 46–54.
- Pan, Y., Dong, P., 1999. The lower Changjiang (Yangzi/Yangtze River) metallogenic belt, east-central China: intrusion-and wall rock-hosted Cu-Fe-Au, Mo, Zn, Pb, Ag deposits. *Ore Geol. Rev.* 15 (4), 177–242.
- Pidgeon, R.T., Bosch, D., Bruguier, O., 1996. Inherited zircon and titanite U-Pb systems in an archean syenite from southwestern Australia: implications for U-Pb stability of titanite. *Earth Planet. Sci. Lett.* 141, 187–198.
- Qin, Y.J., Zeng, J.N., Zeng, Y., Ma, Z.D., Chen, J.H., Jin, X., 2010. Zircon LA-ICP-MS U-Pb dating of ore-bearing pyroxene-trachyanandesite porphyry and its geological significance in Luohu-Nihe iron ore field in Lu-Zong basin, southern Anhui, China. *Geol. Bull. China* 29 (6), 851–862 (in Chinese).
- Qiu, H., 2014. Diagenesis of Intermediate-acidic Intrusive Rock in the Lu-Zong Areas, Anhui Province (Masters Thesis). Hefei University of Technology (in Chinese).
- Ren, Q.J., Liu, X.S., Xu, Z.W., 1991. Mesozoic Volcano Tectonic Depression and Its Mineralizing Process in Lujiang-Zongyang Area, Anhui Province. Geological Publishing House, Beijing, pp. 1–206 (in Chinese).
- Scott, D.J., St-Onge, M.R., 1995. Constraints on Pb closure temperature in titanite based on rocks from the Ungava Orogen, Canada; implications for U-Pb geochronology and P-T-t path determinations. *Geology* 23 (12), 1123–1126.
- Sepahi, A.A., Shahbazi, H., Siebel, W., Ranin, A., 2014. Geochronology of plutonic rocks from the Sanandaj-Sirjan zone, Iran and new zircon and titanite U-Th-Pb ages for granitoids from the Marivan pluton. *Geochronometria* 41 (3), 207–215.
- Smith, M.P., Storey, C.D., Jeffries, T.E., Ryan, C., 2009. In situ U-Pb and trace element analysis of accessory minerals in the Kiruna District, Norrbotten, Sweden: new constraints on the timing and origin of mineralization. *J. Petrol.* 50 (11), 2063–2094.
- Stern, R.A., 1997. The GSC sensitive high resolution ion microprobe (SHRIMP): analytical techniques of zircon U-Th-Pb age determinations and performance evaluation. Radiogenic age and isotopic studies: report 10. *Geol. Surv. Can. Curr. Res.* 1997-F, 1–31.
- Storey, C.D., Jeffries, T.E., Smith, M., 2006. Common lead-corrected laser ablation ICP-MSU-Pb systematics and geochronology of titanite. *Chem. Geol.* 227, 37–52.
- Storey, C.D., Smith, M.P., Jeffries, T.E., 2007. In situ LA-ICP-MS U-Pb dating of metavolcanics of Norrbotten, Sweden: records of extended geological histories in complex titanite grains. *Chem. Geol.* 240 (1–2), 163–181.
- Sun, J.F., Yang, J.H., Wu, F.Y., Li, X.H., Yang, Y.H., Xie, L.W., Wilde, S.A., 2010. Magma mixing controlling the origin of the Early Cretaceous Fangshan granitic pluton, North China Craton: in situ U-Pb age and Sr-, Nd-, Hf- and O-isotope evidence. *Lithos* 120, 421–438.
- Tang, Y.C., Wu, Y.C., Chu, G.Z., 1998. Geology of Copper-gold Polymetallic Deposits in the Along-Changjiang Area of Anhui Province. Geological Publishing House, Beijing, pp. 60–85 (in Chinese).
- Tiepolo, M., Oberti, R., Vannucci, R., 2002. Trace-element incorporation in titanite: constraints from experimentally determined solid/liquid partition coefficients. *Chem. Geol.* 191, 105–119.
- Tropper, P., Manning, C.E., Essene, E.J., 2002. The substitution of Al and F in titanite at high pressure and temperature: experimental constraints on phase relations and solid solution properties. *J. Petrol.* 43, 1787–1814.
- Xie, G.Q., Zhao, H.J., Zhao, C.S., Li, X.Q., Hou, K.J., Pan, H.J., 2009. Re-Os dating of molybdenite from Tonglushan ore district in southeastern Hubei Province, Middle-Lower Yangtze River belt and its geological significance. *Mineral. Deposita* 03, 227–239 (in Chinese).
- Xu, L., Bi, X.W., H, R.Z., Tang, Y.Y., Wang, X.S., Xu, Y., 2015. LA-ICP-MS mineral chemistry of titanite and the geological implications for exploration of porphyry Cu deposits in the Jinsaiyang-Red River alkaline igneous belt, SW China. *Mineral. Petrol.* 109 (2), 181–200.
- Yuan, F., Zhou, T.F., Fan, Y., Zhang, L.J., Tang, M.H., Duan, C., Lu, S.M., Qian, C.C., 2008. Source, evolution and tectonic setting of Mesozoic volcanic rocks in Lu-Zong basin, Anhui Province. *Acta Petrol. Sinica* 24 (8), 1691–1702 (in Chinese with English abstract).
- Zhai, Y.S., Yao, S.Z., Ling, X.D., 1992. Regularities of Metallogenesis for Copper (Gold) Deposits in the Middle and Lower Reaches of the Yangtze River Area. Geological Publishing House, Beijing, pp. 1–120 (in Chinese).
- Zhang, L.J., 2011. Polymetallic Mineralization and Associated Magmatic and Volcanic Activity in the Lu-Zong Basin, Anhui Province, Eastern China (PhD thesis). Hefei University of Technology (in Chinese).
- Zhou, T.F., Fan, Y., Yuan, F., 2008a. Advance on petrogenesis and metallogeny study of the mineralization belt of the Middle and Lower reaches of the Yangtze River area. *Acta Petrol. Sinica* 24 (8), 1665–1678 (in Chinese with English abstract).
- Zhou, T.F., Fan, Y., Yuan, F., Lu, S.M., Shang, S.G., Cooke, D., Meffre, S., Zhao, G.C., 2008b. Geochronology of the volcanic rocks in the Lu-Zong (Lujiang-Zongyang) basin and its significance. *Sci. China (D)* 51 (10), 1470–1482.
- Zhou, T.F., Fan, Y., Yuan, F., Song, C.Z., Zhang, L.J., Qian, C.C., Lu, S.M., Cooke, D., 2010a. Temporal-spatial framework of magmatic intrusions in Lu-Zong volcanic basin in East China and their constraint to mineralizations. *Acta Petrol. Sinica* 26 (9), 2694–2714 (in Chinese with English abstract).
- Zhou, T.F., Fan, Y., Yuan, F., Zhang, L.J., Ma, L., Qian, B., Xie, J., 2011a. Petrogenesis and metallogeny study of the volcanic basins in the Middle and Lower Yangtze metallogenic belt. *Acta Geol. Sinica* 85 (5), 712–730 (in Chinese with English abstract).
- Zhou, T.F., Wu, M.A., Fan, Y., Duan, C., Yuan, F., Zhang, L.J., Liu, J., Qian, B., Franco, P., Cooke, D., 2011b. Geological, geochemical characteristics and isotope systematics of the Longqiao iron deposit in the Lu-Zong volcano-sedimentary basin, Middle-Lower Yangtze (Changjiang) River Valley, Eastern China. *Ore Geol. Rev.* 43, 154–169.
- Zhou, T.F., Fan, Y., Yuan, F., Zhong, G.X., 2012. Progress of geological study in the Middle and Lower Reaches of the Yangtze River Valley metallogenic belt. *Acta Petrol. Sinica* 28 (10), 3051–3066 (in Chinese with English abstract).
- Zhou, T.F., Yuan, F., Yue, S.C., Liu, X.D., Zhang, X., Fan, Y., 2007. Geochemistry and evolution of ore-forming fluids of the Yueshan Cu-Au skarn-and vein-type deposits, Anhui Province, South China. *Ore Geol. Rev.* 31 (2), 279–303.
- Zhou, T.F., Zhang, L.J., Yuan, F., Fan, Y., Cooke, D., 2010b. LA-ICP-MS in situ trace element analysis of pyrite from the Xinqiao Cu-Au-S deposit in Tongling, Anhui, and its constraints on the ore genesis. *Earth Sci. Front.* 17 (2), 306–319 (in Chinese).
- Zhu, Q.Q., Xie, G.Q., Jiang, Z.S., Sun, J.F., Li, W., 2014. Characteristics and in situ U-Pb dating of hydrothermal titanite by LA-ICPMS of the Jingshandian iron skarn deposit, Hubei Province. *Acta Petrol. Sinica* 30 (5), 1322–1338 (in Chinese with English abstract).